

DETERMINATION OF THE DARK MATTER PROFILE OF ABELL 2199 FROM INTEGRATED STARLIGHT¹

DANIEL D. KELSON^{2,3}, ANN I. ZABLUDOFF⁴, K.A. WILLIAMS⁵, S.C. TRAGER^{6,7}, J.S. MULCHAEY⁶,
 AND MICHAEL BOLTE⁵

Accepted for Publication in the Astrophysical Journal

ABSTRACT

We have obtained deep, long-slit spectroscopy along the major axis of NGC 6166, the cD galaxy in the cluster Abell 2199, in order to measure the kinematics of intracluster starlight at large radii. The velocity dispersion initially decreases from the central value of 300 km s⁻¹, to 200 km s⁻¹ within a few kpc, and then steadily rises to 660 km s⁻¹ at a radius of 60 kpc ($H_0=75 \text{ km s}^{-1}\text{Mpc}^{-1}$, $\Omega_m=0.3$, $\Omega_\Lambda=0.7$), nearly reaching the velocity dispersion of the cluster ($\sigma_{A2199} = 775 \pm 50 \text{ km s}^{-1}$). These data suggest that the stars in the halo of the cD trace the potential of the cluster and that the kinematics of these intracluster stars can be used to constrain the mass profile of the cluster. In addition, we find evidence for systematic rotation ($V/\sigma \approx 0.3$) in the intracluster stars beyond 20 kpc. Such rotation is not seen in the kinematics of the cluster members.

The surface brightness and velocity dispersion profiles can be fit using a single component mass model only by making unphysical assumptions about the level of anisotropy for both the stars in the cD galaxy and for the kinematics of the galaxies in the cluster. Two-component mass models for the cD and its halo are subsequently explored using the kinematics of known cluster members as an additional constraint on the total enclosed mass beyond the extent of the stellar kinematics. Under the assumption of isotropy, the observed major-axis kinematics can be reproduced only if the halo, parameterized by a generalized-NFW profile, has a soft core, *i.e.*, $\alpha < 1$ (a generalized-NFW halo with $\alpha = 1$ is excluded due to low implied stellar mass-to-light ratios). This result is inconsistent with the predictions of current N -body simulations for dark matter halos.

To test the consistency of our halo profiles with those derived from strong lensing measurements in intermediate redshift clusters, we calculate the critical radii for tangential arcs, assuming that our best-fit mass models for the Abell 2199 were placed at cosmological redshifts between $0.2 \leq z \leq 0.5$. The calculated critical radii for our best-fit two-component isotropic models range from 5'' to 40'', depending on the assumed source redshift, consistent with the radii for gravitational arcs observed in intermediate redshift clusters.

We also present the results of Monte Carlo simulations testing the general reliability of velocity dispersion measurements in the regime of low S/N and large intrinsic Doppler broadening.

Subject headings: galaxies: elliptical and lenticular, cD, galaxies: kinematics and dynamics, galaxies: stellar content, galaxies: clusters: individual (Abell 2199), galaxies: individual (NGC 6166), (cosmology:) dark matter

1. INTRODUCTION

The question of how mass is distributed in clusters is long-standing (Smith 1935, 1936). Cosmological N -body simulations attempt to address this question and, despite uncertainties in the input physics, robustly predict a universal mass density profile for dark matter halos (Navarro, Frenk, & White 1997; Moore et al. 1999; Ghigna et al. 2000). The spherically symmetric density profile is parameterized by

$$\rho \propto \frac{1}{x^\alpha (x+1)^{3-\alpha}} \quad (1)$$

where $x = r/r_s$, and r_s is the scale radius at which the slope of the density profile transitions to the steep r^{-3} fall-off. Early studies of the universality of the profile suggested $\alpha = 1$ (Navarro, Frenk, & White 1997). While there remains some controversy, more recent simulations indicate $\alpha = 1.5$ (Ghigna et al. 2000). The predictions are based on collisionless N -body simulations, but some attempts to incorporate the effects of gas dynamics have led to steeper inner profiles ($\alpha \lesssim 2$; Tissera & Domínguez-Tenreiro 1998; Alvarez, Shapiro, & Martel 2001). Alternative forms of dark matter have also been explored (e.g.,

¹ Based on observations obtained at the W. M. Keck Observatory, which is operated jointly by the California Institute of Technology and the University of California.

² Department of Terrestrial Magnetism, Carnegie Institution of Washington, 5241 Broad Branch Rd., NW, Washington, DC 20015

³ The Observatories of the Carnegie Institution of Washington, 813 Santa Barbara Street, Pasadena, CA 91101

⁴ Steward Observatory, University of Arizona, Tucson, AZ 85721

⁵ UCO/Lick Observatory, Department of Astronomy and Astrophysics, University of California, Santa Cruz, CA 95064

⁶ The Observatories of the Carnegie Institution of Washington, 813 Santa Barbara Street, Pasadena, CA 91101

⁷ Hubble Fellow

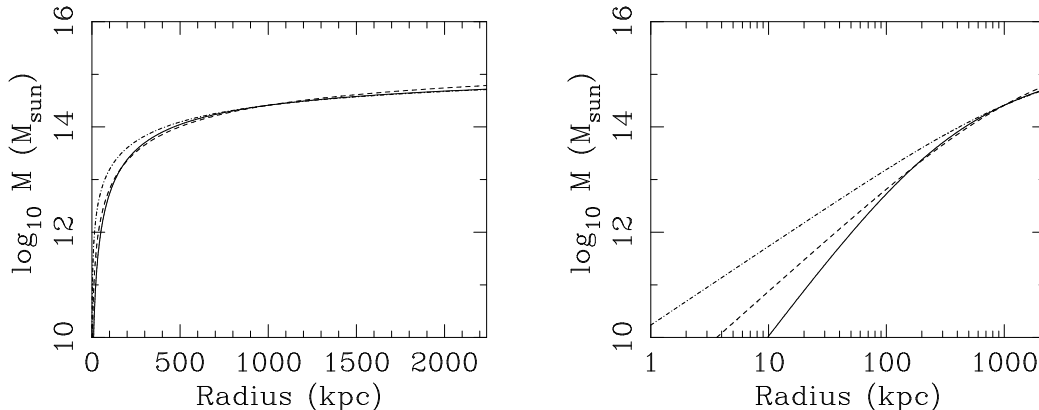


FIG. 1.— Mass profiles for generalized NFW dark matter halos with $\alpha \in \{0, 1, 1.5\}$ (solid, dashed, dot-dashed, respectively). These mass profiles have been renormalized to have identical mass at 1 Mpc. The left and right panels are identical, except for the linear and logarithmic stretch in radius. Note the range of projected radii, $R \lesssim 100$ kpc, over which one would observe significant differences.

Spergel & Steinhardt 2000; Firmani et al. 2001; Colín et al. 2000). Halos of self-interacting dark matter have soft, uniform density cores ($\alpha < 1$; Yoshida et al. 2000; Davé et al. 2001), but their low ellipticities are considered problematic (e.g., Miralda-Escudé 2002).

Some CDM simulations indicate that α itself may be a function of halo mass, with cluster-sized halos tending to $\alpha = 1$ and galaxy-sized halos tending to $\alpha = 1.5$ (Jing & Suto 2000, though see Klypin et al. (2001)). Such results suggest that the density profiles of dark matter halos are quite sensitive to their histories of formation, accretion, and merging, as well as to the initial conditions of collapse (Nusser & Sheth 1999), and these notions are tested explicitly by Weinberg (2001), who finds that noisy evolutionary processes can drive halo profiles to a uniform shape with soft cores. This result appears similar to the profile derived by Iliev & Shapiro (2001), wherein the collapse of spherical top-hat density perturbations was shown to produce truncated isothermal spheres, i.e., $\alpha = 0$. The solutions of Iliev & Shapiro (2001) and Weinberg (2001) may naturally produce soft cores because of the boundary condition of finite phase-space densities at $r = 0$. This restriction on the solutions to the Lane-Emden or Fokker-Planck equations (Iliev & Shapiro 2001; Weinberg 2001) runs counter to the basic assumption in fitting Eq. 1 to N -body profiles, wherein the central phase-space densities are allowed to diverge (Taylor & Navarro 2001).

While such analytic work is providing insight into the physics of dark matter halo evolution, there are few observational constraints on cluster scales to test the $1 \leq \alpha \leq 1.5$ models routinely assembled by the simulations. For the massive dark matter halos of rich clusters, this range in α yields models that are quite similar outside of $\lesssim 100$ kpc, where most cluster-related observations have weight. Figure 1 shows the mass profiles of example generalized-NFW mass profiles for $\alpha \in \{0, 1, 1.5\}$. The two panels show the mass profiles using linear and logarithmic stretches in cluster radius and illustrate the need for observations within the inner $\lesssim 100$ kpc in order to measure the inner slope of the dark matter halo profile (see also Klypin et al. 2001).

Observational tests at these small radii are scarce. The determination of the mass profile from kinematics of clus-

ter galaxies within this region has been difficult because there are generally few members. van der Marel et al. (2000) attempted to solve this problem by combining the redshifts from the CNOC1 cluster survey (Yee, Ellingson, & Carlberg 1996) into a single fiducial cluster. They argued that the best-fit mass profiles were described by $\alpha \approx 1$, but their analysis did not take into account the contribution of the stellar mass of any brightest cluster galaxies (BCG) to the total mass profile of the fiducial cluster. An accurate determination of mass profiles of the inner 100 kpc for clusters from X-ray observations has been hampered to date by poor spatial resolution, and by the presence of cooling flows and shocked regions. Even as X-ray observations improve, uncertainties about the mass contributions from BCGs will persist (see Arabadjis, Bautz, & Garmire 2001). Still another method, that of using the kinematics of planetary nebulae and/or globular clusters (e.g., Cohen & Ryzhov 1997; Côté et al. 2001), requires painstaking identification and spectroscopy of 20-200 discrete objects, and Hernquist & Bolte (1993) show that the resulting inferred mass profiles are subject to large ($>$ factors of 2) uncertainties with such small samples. Strong gravitational lensing measurements can allow one to infer the total surface mass density within the Einstein radius but these constraints are susceptible to degeneracies (Gorenstein et al. 1988) and to uncertainties in the details of the potential (Bartelmann et al. 1995). The mass profile can be better-constrained when there are several arcs, but the brightest cluster galaxies may themselves dominate the shapes of the total surface mass density profile, as may be the case in MS2137-2353 (Hammer et al. 1997). Weak lensing measurements are even less effective at constraining the inner mass profile, given the typical number densities of background galaxies as well as the comparatively large surface areas covered by the galaxies in cluster cores (Hoekstra et al. 1998).

A more promising method for constraining the mass profiles in the cores of rich clusters is to use the kinematics of stars in the extended halos of central cD galaxies (“intracluster starlight”). Past efforts to trace the stellar velocity dispersion profile of IC 1101, in the cluster A2029, to tens of kpc showed that $\sigma(r)$ rises from 400 km s^{-1} to

FIG. 2.— A log-stretch of a B -band image of NGC 6166 with the position of the LRIS long-slit shown for the primary integrations (totaling 7200 s). The radial bins, from which the galaxy spectra were extracted, are shown. Note the increasingly large apertures from which the two-dimensional spectra were summed to achieve adequate signal-to-noise ratio. A second long-slit position, exposed for 1400 s, was also obtained with the slit centered on the galaxy nucleus.

600 km s^{-1} towards larger radii (Dressler 1979; Carter et al. 1985; Sembach & Tonry 1996). Of the many BCGs investigated over radii of $10'' - 20''$, only IC1101 (Fisher, Illingworth, & Franx 1995; Kronawitter et al. 2000) and NGC 6166 (Carter, Bridges, & Hau 1999) have shown such a rise. Such results suggest that the stars in a cD's halo respond to the potential of the cluster.

In this paper we report on a pilot study in which we targeted NGC 6166, the giant elliptical in the center of the rich cluster Abell 2199 ($z = 0.03$), with the Keck II 10m telescope and the Low Resolution Imaging Spectrograph (Oke et al. 1995, ; LRIS). Several factors make this galaxy an ideal choice: (1) it is at rest with respect to the center of the cluster potential (Zabludoff et al. 1990); (2) the cluster itself appears relaxed in X-rays; (3) the presence of a cooling flow in the cluster core suggests little or no recent merger activity in the cluster center; (4) the useful features in its spectrum (e.g., the G-band) do not overlap any strong night-sky emission lines or absorption lines; (5) the redshift allows the $170''$ LRIS slit to subtend 100 kpc ($H_0 = 75 \text{ km s}^{-1} \text{ Mpc}^{-1}$, $\Omega_M = 0.3$, and $\Omega_\Lambda = 0.7$; used throughout this paper); and (6) its declination of 39° makes it observable for most of the night from Mauna Kea. The telescope's large aperture makes it possible to obtain spectra with sufficiently high S/N ratios in the low surface brightness halo of the galaxy while using a narrow slit-width (both to achieve moderate resolution and to exclude interloping galaxies).

We structure the paper as follows. In §2 we discuss the observations and data reduction. The stellar mass density profile is constrained in §3 through the use of the B - and R -

band surface brightness profiles, and the major-axis kinematics of NGC 6166 are derived in §4. In §5 we discuss the reliability of velocity dispersion measurements in the regime of low S/N and large intrinsic Doppler broadening using Monte Carlo simulations. Section 6 discusses the fit of simple mass models to the kinematics of NGC 6166 and Abell 2199, as constrained by the kinematics of cluster members. The implications of our best-fit mass models are discussed in §7 and our conclusions are summarized in §8.

2. OBSERVATIONS AND DATA REDUCTION

The primary goal of this work is the accurate measurement of the second moment (σ) of the line-of-sight velocity distribution (LOSVD) as a function of position along the major-axis of NGC 6166. By combining the σ profile with broad-band imaging, we can obtain constraints on the total mass-to-light (M/L) profile of the galaxy and the inner portions of the surrounding cluster. In this section we describe the B - and R -band imaging of NGC 6166 and its halo, the long-slit spectroscopy, and the processing required to derive the chief products: the surface brightness profile, $\mu(R)$, and the projected line-of-sight velocity dispersion profile, $\sigma(R)$. Using the cosmological parameters given in §1, the scale on the sky is 0.56 kpc/arcsec.

2.1. The Photometry

Three B -band images of NGC 6166, totaling 1870 seconds, and six R -band images, totaling 1280 seconds, were obtained with LRIS during the nights of 30-31 May 1998. The images span 6×8 square arcmin, corresponding to

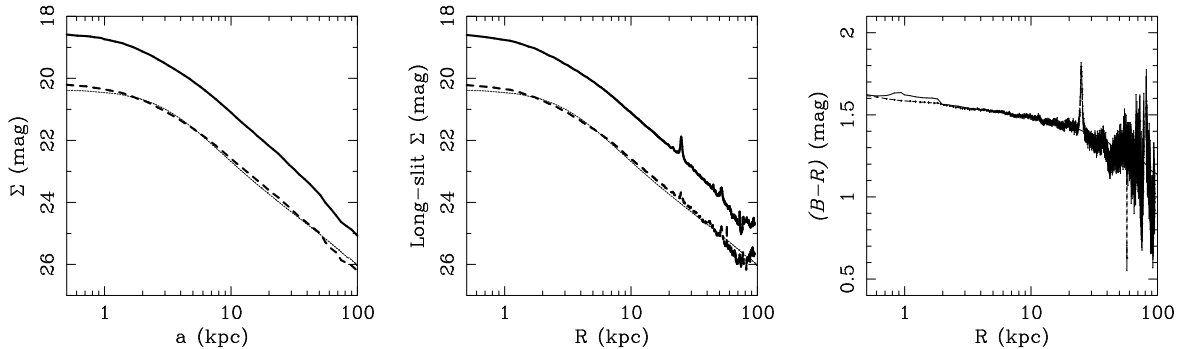


FIG. 3.— (left) The mean R - (solid) and B -band (dashed) surface brightness profile of NGC 6166, derived from isophote fitting, as a function of the major-axis of the isophote. (middle) The R - and B -band surface brightness profile of NGC 6166, derived along the position of the LRIS long-slit. The dotted line in both panels indicates the King model that best fits the B -band profile as measured along the position of the long-slit (see §6. The fit of the King profile was restricted to radii $2''.5 < r < 125''$ ($1.2 \text{ kpc} < r < 70 \text{ kpc}$) and satisfactorily matches the profiles determined from the isophotes and from the long-slit position. (right) The $B - R$ color gradients derived from the isophote fitting (solid line) and the long-slit position (dashed line). Note that the cD becomes bluer with projected radius. The color gradient is indicative of a radial variation in the metallicities and/or ages of the stellar populations and implies that the stellar M/L ratio is also varying with projected radius.

a distance along the major axis of 170 kpc. The seeing during the run was approximately 0.8 arcsec (FWHM). A subsection of the B -band image is shown in Figure 2.

2.1.1. The Surface Brightness Profile

The sky background was determined for each image using the corners of the image furthest from the galaxy, and the sky brightness was then subtracted from the entire image (in both bands). While errors in the sky will severely affect the derived surface brightness profile of the galaxy at radii approaching the extent of the imaging field-of-view, the accuracy in our estimate of the sky is suitable for deriving the surface brightness profile over the extent of the LRIS long-slit ($\sim 3'$). The B - and R -band sky brightnesses were approximately $\mu_{B,sky} = 21.9 \text{ mag/arcsec}^2$ and $\mu_{R,sky} = 20.6 \text{ mag/arcsec}^2$, respectively.

The fitting of elliptical isophotes was performed using the ELLIPSE package of STSDAS in IRAF. The detection of 15 interloping galaxies necessitated modeling (using the ellipse package) and subtraction of their light from the images in both bands. Isophotes were fit to these galaxies, as well as to the cD, and iteratively subtracted from the image. The envelope of one interloper intersects the major-axis between 2 kpc and 14 kpc at a mean level of about 15% of the cD surface brightness. The residuals from the subtraction of this particular interloper amounted to $\sim 5\%$ of the cD surface brightness at those radii along the major-axis. Such residuals were efficiently rejected by the sampling criteria in the final ellipse-fitting of the cD.

2.1.2. The Calibration

We calibrated the B -band photometry using secondary standard stars in the Galactic globular cluster M92, with an error in the photometric zero-point of $\pm 0.016 \text{ mag}$. Calibrating the R -band photometry was problematic because the LRIS filter wheel had not properly inserted the (Johnson) R filter into the optical path for the M92 calibration image. As a result we used the Cousins R -band surface brightness profile from Postman & Lauer (1995) to calibrate our data. The Postman & Lauer (1995) profile

was first transformed from Cousins R to Johnson R using $R_J - R_C = -0.11$ (a good approximation for the spectral energy distributions of old E/S0s; (Fukugita, Shimasaku, & Ichikawa 1995)). We then determined the photometric offset between the LRIS profile and the transformed Postman & Lauer (1995) profile over the radial range of 5 to 40 arcsec. The *rms* of this offset was 0.017 mag.

The B -band extinction to NGC 6166, as estimated by Schlegel et al. (1998), is $A_B = 0.05 \text{ mag}$ ($A_B = 0.00 \text{ mag}$ from Burstein & Heiles 1982). Because this prediction is quite low and irrelevant for the determination of the mass profile we have made no correction for the foreground extinction (it only affects the deduced stellar M/L ratios at a level of $\lesssim 5\%$). The final B - and R -band surface brightness profiles are shown in the left panel of Figure 3.

2.1.3. The Surface Brightness Profile along the LRIS Long-Slit

While isophote fitting provides the maximum signal-to-noise ratio in the surface brightness profile at a given radius, our kinematic profile will be derived along a fixed position angle (the major-axis). Thus it is more appropriate to use the surface brightness profile along this position angle in modeling the mass profile and constraining the mass model of the cD and its halo.

We calculated the B - and R -band slit profiles from eight columns of the CCD image centered on the galaxy nucleus. The long-slit intensities were derived by averaging the eight columns of the slit position in order to produce a single intensity per pixel for each row along the slit. These B - and R -band long-slit surface brightness profiles are shown in the middle panel of Figure 3. The profiles in the right- and left-hand panels are virtually identical because there was very little twisting of the isophotes with radius. Thus our mass modeling will be insensitive to the choice of the long-slit or isophote profile. For the remainder of the paper, we use the profile derived at the position of the LRIS long-slit.

2.1.4. The Color Gradient in NGC 6166

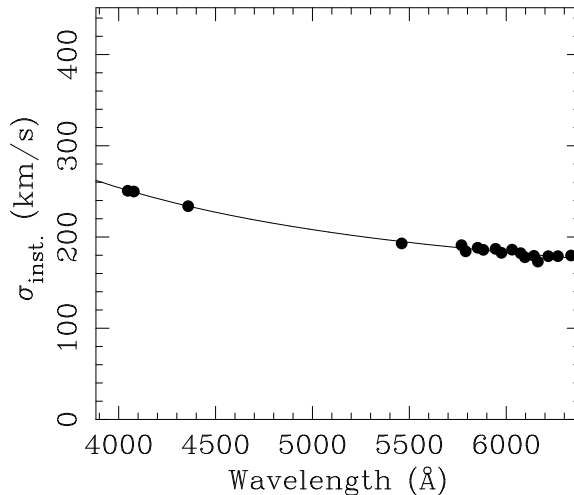


FIG. 4.— The instrumental resolution for the LRIS configuration used for the work presented in this paper. The resolution was determined from the widths of the emission lines from the mercury, krypton, and neon lamps.

The right-hand panel of Figure 3 shows the $B - R$ color gradients derived from both the isophote fitting (solid line) and for the long-slit position (dashed line). The color transitions smoothly from $B - R = 1.6$ mag in the inner regions of the cD to $B - R = 1.4$ mag at $r = 20$ kpc to $B - R = 1.2$ mag at $r = 50$ kpc. These are colors which are typical for E/S0, Sa, and Sbc galaxies, respectively (Fukugita, Shimasaku, & Ichikawa 1995). We find that the gradient is well fit by the second-order polynomial:

$$(B - R) = 1.58 - 0.10[\log r(\text{kpc})]^2 \quad (2)$$

with an *rms* scatter of 0.018 mag.

In §3 we derive structural parameters from the surface photometry and discuss the use of the color gradient to estimate possible variations in stellar M/L with projected radius.

2.2. The Spectroscopy

The primary spectroscopic data consist of four 40 minute exposures of the galaxy, flanked by five 40 minute offset-sky exposures (taken before and after the on-galaxy exposures). We used the $1''.5$ wide long-slit with the 600 grooves mm^{-1} grating, blazed at 5000Å. The spectral coverage extends from 3800Å to 6400Å. The resolution of ~ 7 Å FWHM is equivalent to $\sigma_{\text{inst.}} \approx 200$ km/s, as shown in Figure 4, more than adequate to resolve the velocity dispersions in the cD and its halo. While the spectral coverage is suitable for deriving absorption line velocity dispersions from several features, *e.g.*, the Mg b, G-band, or Ca H & K, we concentrated our efforts around the G-band as a compromise between the desires to minimize contamination due to the sky background and to achieve adequate signal-to-noise ratios.

To maximize the extent of the halo observed and still preserve radial profile information for NGC 6166, we placed one end of the long-slit at the galaxy center and the rest of the $170''$ long-slit north-east along the major axis at a position angle of 33 degrees (see Figure 2). Our imaging of NGC 6166 on the same night confirms this angle as that of the major axis to within a degree. A second

position, at the same position angle but centered on the galaxy nucleus, was also obtained in 1400 sec of integration time.

Because NGC 6166 fills the entire length of a long-slit placed long the major-axis, we obtained alternating sky pointings offset from the galaxy, similar to the approach used by Dressler (1979), to facilitate accurate removal of the sky background. In principle, obtaining the sky spectrum at the same position on the detector as the galaxy spectra should minimize the effects of imperfect flat fielding, errors in rectification, and uncertainties in interpolating the sky background from the slit ends. While Sembach & Tonry (1996) used charge shuffling and chopping of the telescope on 5 min timescales in order to ensure that the offset-sky spectra were obtained at precisely the same physical pixel locations as the galaxy spectra, LRIS cannot be used exactly in this mode. Therefore we chose to nod between galaxy and sky on 40 min intervals, having to read out the detector at each position/exposure. Our exposure times were chosen as a compromise between (1) requiring the data in the low-surface brightness halo of the cD to be limited by the noise in the sky background and not by the read noise in the electronics, and (2) avoiding the time-variability of the background. Despite the variability of the sky spectrum, and the flexure characteristics of the instrument, we were able to obtain quality halo spectra where the surface brightness of the galaxy is approximately 6% of sky (see below).

2.2.1. Rectification and Wavelength Calibration

We used the software package EXPECTOR (Kelson et al. 2000) to rectify and wavelength-calibrate the LRIS spectroscopic data. A combination of Hg, Kr, Ne, and Ar lamps allowed us to rectify the spectra and to derive the high order terms for the wavelength calibration. The *rms* scatter about the dispersion solution of the lamp spectra was 0.04Å (3 km s^{-1} at the G band). The zero-points of the dispersion solutions of the galaxy spectra were refined

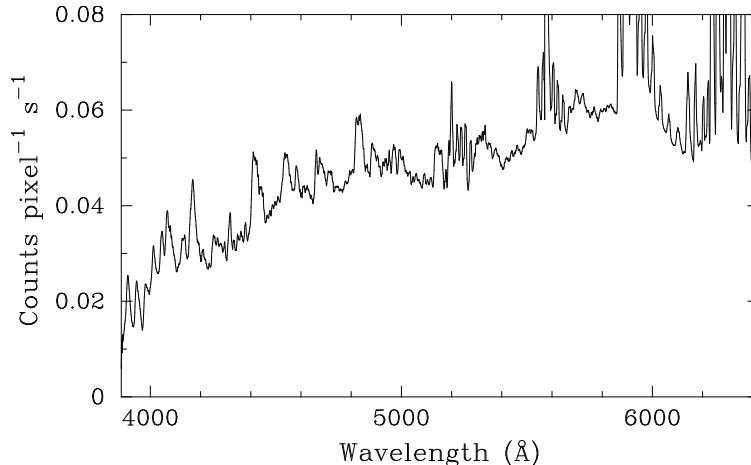


FIG. 5.— A spectrum of the Mauna Kea night sky in the blue. Note the tremendous amount of structure blueward of O I 5577Å, including the (strongly variable) nitrogen line at 5199Å, which is superposed on OH Q & R lines at ~ 5200 Å. Because most of the features are broad with very sharp edges, poor sky subtraction of low-surface brightness sources can artificially alter the broad absorption features intrinsic to a galaxy spectrum.

using several high S/N sky emission lines (e.g., 5224Å, 5238Å, 5577Å, 6300Å), resulting in a final rms scatter of 0.6 Å (± 40 km s $^{-1}$ at the G-band). This large residual scatter about the sky lines is typical for LRIS data largely because the lines in lamp spectra are asymmetric compared with the sky emission lines. The asymmetries in the line profiles systematically vary with position across the CCD causing small systematic errors in the measurements of the line centers, and thus introduce a bias in the wavelength scale (Kelson et al. 2000). These large residuals appear as a moderate-order deviation from the lamp line dispersion solution and may be reduced with further work if one intends to utilize a very long spectral baseline (see Kelson et al. 2000). If the direct fitting of broadened templates to the galaxy spectrum is performed over a relatively short wavelength range, then a moderate rms in the dispersion solution manifests itself primarily as a zero-point error, and secondarily as a much smaller effective rms scatter in a local dispersion solution. For our data and fitting range, the effective scatter is smaller by a factor of four (to ± 10 km s $^{-1}$), and thus has a negligibly small impact on the measured velocity dispersions.

2.2.2. Background Subtraction

By obtaining full 2D sky spectra at offset positions from the cD, before and after each galaxy exposure, one should, in principle, be able to reconstruct the sky background at the time of the galaxy exposures. We modeled the temporal variability in the sky by fitting low-order polynomials to the sky values at each pixel, as functions of time and/or airmass. This method should have produced the expected 2D spectra of the sky background at the time and/or airmass of the galaxy observations, but such simple algorithms and interpolations did not allow for sufficiently accurate subtraction of the variable sky spectrum (even in the blue; see Figure 5).

We improved the background subtraction by fitting each CCD row in the on-galaxy 2D exposures using Equation 8 of Kelson et al. (2000), originally suggested for measuring

velocity dispersions from data from which the background has not been subtracted. By doing so, each CCD row in the data was fit as a sum of (1) the high signal-to-noise sky spectrum (from the offset sky-exposures in the same CCD row), (2) a broadened velocity dispersion template, and (3) the low-order continuum functions. Thus, the data were represented by a sum of the galaxy’s contribution with the spectrum of the night sky, scaled by and offset by low-amplitude and low-order polynomials. This polynomial, equivalent to $< 1\%$ errors in the sky determination, effectively removes the time-variability of the sky background and any instabilities in the instrument. Additional broadening of the sky spectrum did not improve χ^2 so we infer that focus variabilities were negligible. Construction of the background in this way provides a high signal-to-noise map of the contribution of the sky spectrum to the data within each row. At large galactic radii, where the galaxy contributes very little flux, this construction of the row-to-row map of the background produces a noisy row-to-row map of galaxy flux. Therefore, the 2D map of the sky contribution was fit by a low order polynomial in each wavelength bin and this spatially smoothed map of the sky background was used to perform the background subtraction. Based on the analysis in §5, in which we discuss the robustness of the σ measurements, our results are not sensitive to any remaining uncertainties in the background subtraction.

2.2.3. Extraction

Spectra were summed along the spatial direction of the CCD in order to produce 1D spectra with adequate signal-to-noise ratios (≥ 20 per Å) for determination of velocity dispersions. Figure 2 illustrates the positions of the end-points of the spatial bins using short solid lines perpendicular to the length of the slit. In Figure 6 we show the total sky+galaxy spectra from the deep spectroscopic integrations of the cD halo in four representative bins along the major-axis. The corresponding sky-subtracted galaxy spectra are shown in the right-hand panels of Figure 6.

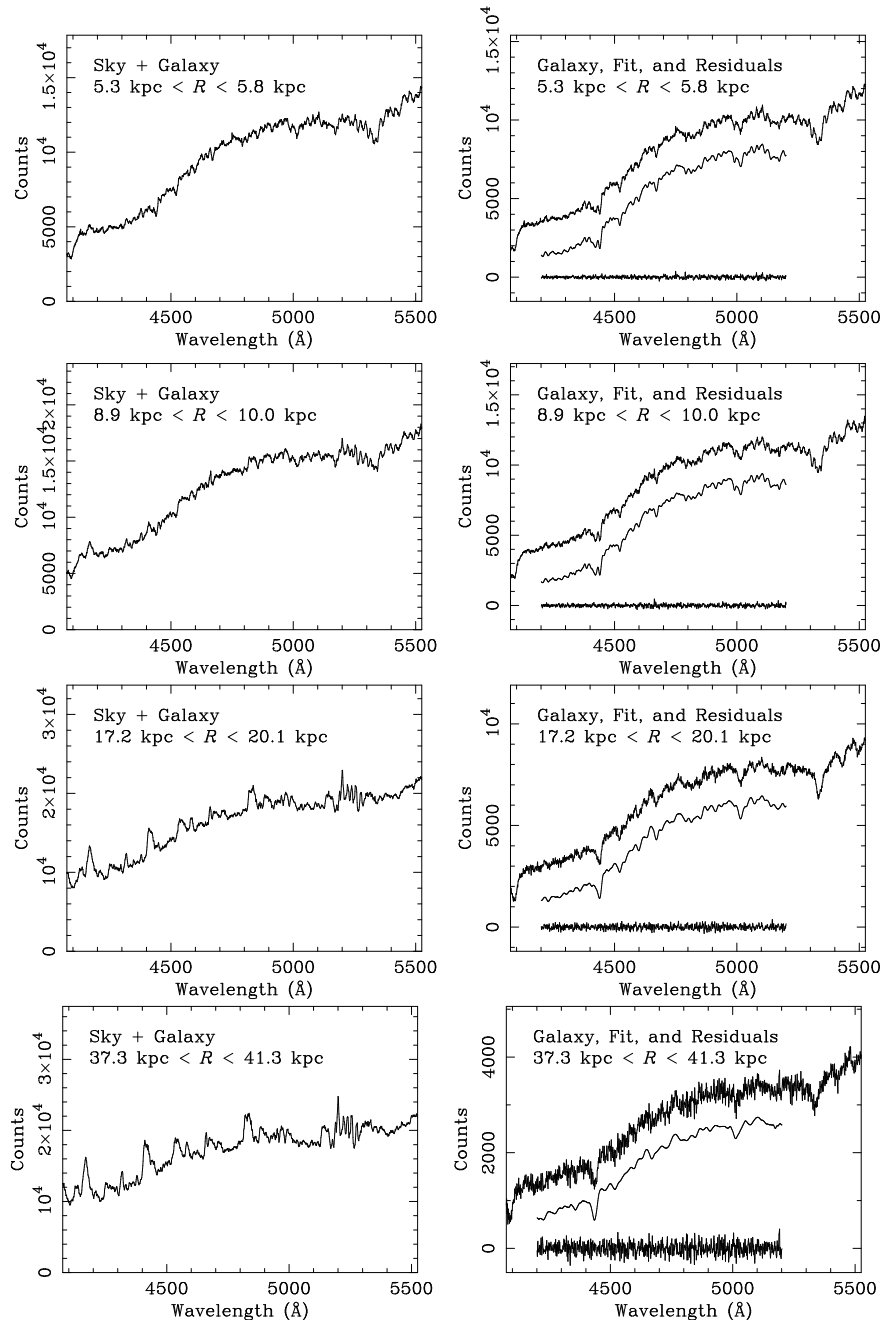


FIG. 6.— The left-hand panels show the total sky + galaxy spectra in four representative bins in projected radius along the major axis of NGC 6166. The right-hand panels show the galaxy spectra extracted from the same radial bins. The velocity dispersion fits, shown below the galaxy spectra, illustrate the quality of the fitting method. The residuals from each fit are also shown and these indicate that no significant systematic effects remain unaccounted.

The data have not been flux-calibrated.

3. CONSTRAINTS ON THE STELLAR LUMINOSITY DENSITY

In constructing mass models for NGC 6166, the density profile of the stellar mass component is constrained by the observed surface brightness profile. The surface brightness profile only constrains the shape of the stellar luminosity density profile; the stellar M/L ratio (M/L_*) can only be constrained by the kinematics. Traditionally, photometry from a single bandpass is used, with the assumption of a spatially invariant M/L_* . However, galaxies have gradients in their stellar populations (e.g., Peletier et al. 1990;

Franx, Illingworth, & Heckman 1989; Davies, Sadler, & Peletier 1993; González 1993; Fisher, Franx, & Illingworth 1996; Kuntschner 1998; Trager et al. 2000) and by inference must have gradients in M/L_* . Fortunately, we have surface photometry in both B and R , and in this section we combine the $B - R$ color gradient from §2.1.4 with simple stellar population synthesis models to estimate the gradients in the B -band M/L_* ratio (M/L_B) and R -band M/L_* ratio (M/L_R).

While the nature of the color gradient (as a spatial variation in stellar ages and/or in stellar chemical abundances) remains uncertain, we can make some simple assumptions

to test to what extent the gradient in the stellar mass-to-light ratio will affect our conclusions about the profile of gravitational mass in the system. We explore *three* extreme cases: (1) no gradient in the properties of the stellar population; (2) a gradient in $[\text{Fe}/\text{H}]$; and (3) a gradient in stellar ages. Using the Vazdekis et al. (1996) models, we have derived the correlation of $(B - R)$ color with M/L_B and M/L_R at fixed age or at fixed metallicity:

$$\begin{aligned} \Delta \log(M/L_B)|_{\text{fixed age}} &= 0.96\Delta(B - R) \\ \Delta \log(M/L_R)|_{\text{fixed age}} &= 0.56\Delta(B - R) \end{aligned} \quad (3)$$

and

$$\begin{aligned} \Delta \log(M/L_B)|_{\text{fixed } [\text{Fe}/\text{H}]} &= 2.00\Delta(B - R) \\ \Delta \log(M/L_R)|_{\text{fixed } [\text{Fe}/\text{H}]} &= 1.60\Delta(B - R). \end{aligned} \quad (4)$$

Combining the above relations with the color gradient in NGC 6166, we find that the adoption of a constant M/L_B would lead one to overestimate the stellar mass densities at large radii by factors of 2–6. By incorporating the gradient in stellar populations, we hope to derive (presumably) more accurate representations of the stellar mass density profile (though the results would still be dependent on the assumption of the age- or metallicity-dependence of the color gradient).

In Table 1 we list the parameters of the best-fit de Vaucouleurs, King (1966), and power-law profiles, under the three extreme assumptions about the gradient in the stellar populations (the power-law profile is assumed to be of the form: $\rho \propto [1 + (r/r_c)^2]^\gamma$). All three parameterizations fit the data well, with *rms* residuals between 0.03 and 0.07 mag.

When fitting the model profiles to the uncorrected B - and R -band surface brightness profiles, one obtains smaller effective and core radii in the redder bandpass, consistent with the stellar populations becoming bluer with increasing radius. When the B - and R -band surface brightness profiles are corrected, the resulting structural parameters from the two bandpasses are essentially identical. Because

we have divided our observed surface brightness profiles by the gradients in M/L_B and M/L_R , the corrected surface density profiles should more accurately reflect the stellar mass density profile (modulo the normalization by a constant).

As an aside, there are large differences in the values of r_e obtained from the uncorrected, age-variation-corrected, and metallicity-variation-corrected profiles. In the case where the stellar population gradient of NGC 6166 (and presumably of other giant ellipticals) is due solely to gradients in the chemical abundances, the deduced half-mass radius is smaller than the B - and R -band half-light radii by 45% and 30%, respectively. Such large systematic errors in the half-mass radii of elliptical galaxies may have a grave impact on early-type galaxy scaling relations, such as the fundamental plane (Faber et al. 1987; Djorgovski & Davis 1987), through the strongly correlated errors in r_e and μ_e and the modest scatter in the color gradients of ellipticals and S0s (e.g., Peletier et al. 1990). For the work presented here, we do not utilize the half-light or half-mass radii, so we offer this short discussion simply as a cautionary note.

Now that we are free from the assumption of a constant stellar mass-to-light ratio, we can explore to what extent the stellar mass may or may not be sufficient to support the motions of the stars through the cD halo.

4. THE MAJOR-AXIS KINEMATICS OF NGC 6166

Spectra for the galaxy were extracted from the radial bins defined in Figure 2. Four representative spectra are shown in the right-hand panels of Figure 6. In each of the radial bins, $S/N \geq 20$ per \AA , with the S/N reaching 120 per \AA inside 15 kpc. With such S/N ratios, the data are quite suitable for measuring the internal motions of the stars in NGC 6166 and its halo out to 60 kpc. To simplify the derivation of the internal kinematics, we parameterize the LOSVD as a Gaussian. In the inner regions the

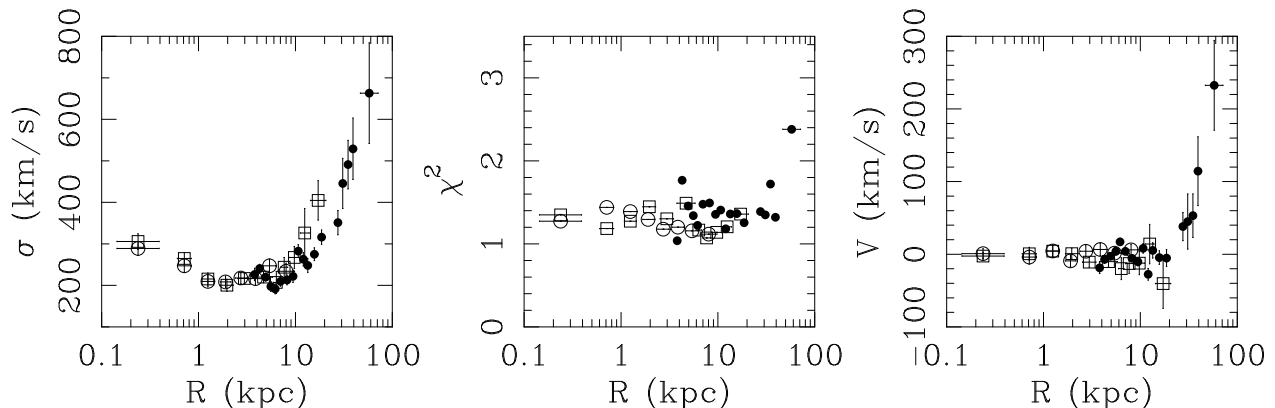


FIG. 7.— (left) The observed projected velocity dispersion profile of NGC 6166 derived from the deep, off-set long-slit pointing (filled circles), and from the shallow, central long-slit exposure (open circles and squares). The squares indicate the profile from the opposite side of the galaxy from the filled circles, with the projected radii flipped for comparison. The open and closed circles between 4 kpc $\lesssim R \lesssim$ 12 kpc were obtained by simultaneously fitting both the primary (NGC 6166) and secondary (interloper at +1300 km/s) component. Note that the velocity dispersion profile has a large positive gradient in σ on both sides of the galaxy after a decline from the central value of $\sigma_0 = 300$ km/s. (center) The reduced χ^2 as a function of position. Our methods provide excellent fits to the NGC 6166 spectra except in the outermost bin, where the galaxy surface brightness is 6% of the sky in the B -band. Between 4 kpc $\lesssim r \lesssim$ 12 kpc the low reduced χ^2 values indicate that the interloping galaxy at $\delta v = +1300$ km/s was successfully removed in the fitting procedure and had negligible impact on the velocity dispersions measured for NGC 6166. (right) The rotation curve from the same data. Note the apparent increase in rotation in the outskirts of the cD.

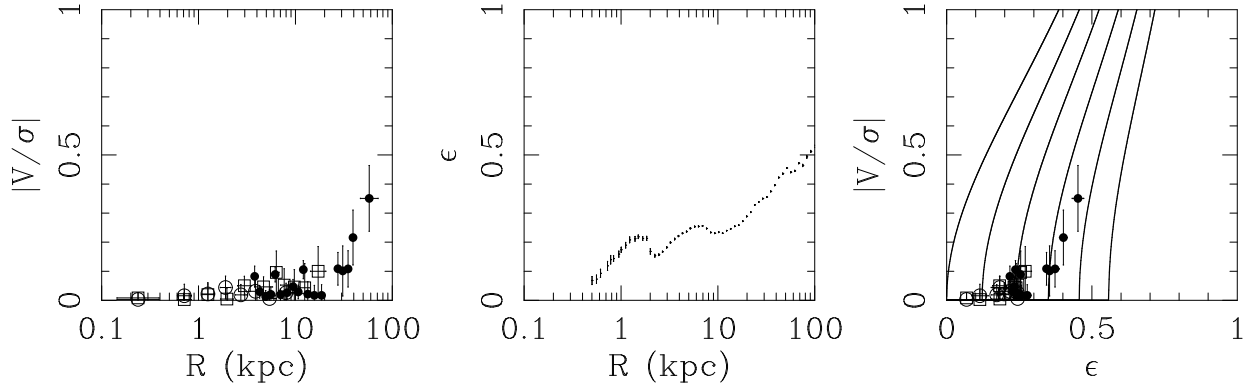


FIG. 8.— (left) The level of rotational support as a function of projected radius along the major-axis (symbols as in Fig. 7. Most of the stars in NGC 6166 are clearly supported by random motions with an apparent increase in rotational support outside of $R = 20$ kpc. (center) The ellipticity of the B -band isophotes as a function of projected radius along the major-axis. The isophotes of NGC 6166 become increasingly elliptical at large radii, consistent with an increase in rotational flattening. (right) The level of rotational support as a function isophote ellipticity in the B -band. The curves show the expected correlations between $|V/\sigma|$ and ϵ for rotationally supported oblate spheroids with $\delta \equiv 1 - \sigma_{zz}/\sigma_{xx} \in \{0, 0.1, 0.2, 0.3, 0.4, 0.5\}$ observed edge-on. Using these data we conclude that within a projected radius $R \lesssim 20$ kpc NGC 6166 is not a rotationally flattened oblate spheroid. Beyond projected radii $R = 20$ kpc, the isophotes become more elliptical and the cD halo appears to become mildly anisotropic and rotationally flattened. This level of rotational flattening only amounts to $\lesssim 5\%$ of the kinetic energy in the halo and has little effect on our results.

high S/N ratios would normally have allowed us to measure the higher-order moments h_3 or h_4 of the LOSVD (van der Marel & Franx 1993). Unfortunately (see below), an interloping object with a velocity shift of 1300 km/s from NGC 6166 contaminates its spectrum between 4 kpc $\lesssim r \lesssim$ 12 kpc. As a result the LOSVDs for both objects were modeled by pure Gaussians, with both components being fit simultaneously (e.g., Kelson et al. 2000). At large radii in the cD halo, where accurate determinations of h_3 or h_4 would also be useful for constraints on the anisotropy, the S/N ratios are not sufficient. However in other giant ellipticals the departures of LOSVDs from Gaussian are typically small, even at large radii (e.g., Kronawitter et al. 2000).

For each extracted spectrum, we performed a least-squares fit of broadened template spectra, using stellar template spectra from the literature (Kelson et al. 2000) and a more narrow range of stellar spectra obtained during the observing run. Using the procedures outlined in Kelson et al. (2000), we use night-sky air-glow emission lines and calibration lamp lines to measure the instrumental broadening. Once the instrumental broadening had been characterized as a function of wavelength and position along the CCD, the template spectra from the literature were broadened to match the instrumental resolution of the galaxy spectra. While we relied primarily on the templates from the literature to derive the internal kinematics, the template spectra obtained during the run were useful to verify the robustness of our measurements. The velocity dispersions derived using the templates observed during the run agreed with velocity dispersions derived using the templates from the literature at the level of 0.5%.

The quality of the fits to the galaxy spectra can be seen in the right-hand panels of Figure 6. While the interloper is clearly visible in two of the examples in the figure, the contamination was easily removed by the fitting procedures and the residuals of the fits show no remaining systematic effects. The other two radial bins shown

in the figure show the quality of the velocity dispersion fits at large projected radii ($17.2 \leq R \leq 20.1$ kpc and $37.3 \leq R \leq 41.3$ kpc).

In the left panel of Figure 7, we use filled circles to show the velocity dispersion profile derived from the deep, primary long-slit observations on one side of the galaxy (see Figure 2). The open points (circles and squares) show the data from the shallow central pointing; the open circles are from the same side of the galaxy as the deep pointing, and the open squares were derived from the opposite side of the galaxy. The agreement of $\sigma(R)$ from both sides of the galaxy is excellent and indicates that the interloping galaxy was successfully removed during the fitting of the deep spectroscopy. The reduced χ^2 values, shown in the central panel, show the quality of the velocity dispersion fits.

In the deep spectroscopy of the cD halo there is evidence for a significant level of rotation beyond $R \gtrsim 30$ kpc, consistent with the results of Carter, Bridges, & Hau (1999) to $R \sim 20$ kpc. The right panel of Figure 7 shows the stellar rotation curve and the fraction of rotational support ($|V/\sigma|$) as a function of projected radius is shown in the left-hand panel of Figure 8.

The error bars shown in the figures represent the formal uncertainties only. Despite the 18% formal uncertainty and elevated χ^2 in the last radial bin, the gradient in σ is clearly significant and is also consistent with the profile of Carter, Bridges, & Hau (1999) to $R \lesssim 20$ kpc. Additional errors, such as those arising from template mismatch, are estimated at ~ 3 -5% by comparing the velocity dispersions using templates of varying spectral types. Errors in σ due to background subtraction are included in the estimates of the formal uncertainties (verified by using the χ^2 minimization described in §5.2.4 of Kelson et al. 2000). The implications of the major-axis kinematics for the mass profile of NGC 6166 will be discussed in §6.

Table 2 lists the major-axis kinematics for NGC 6166. The columns are as follows: (1) the central radius of the

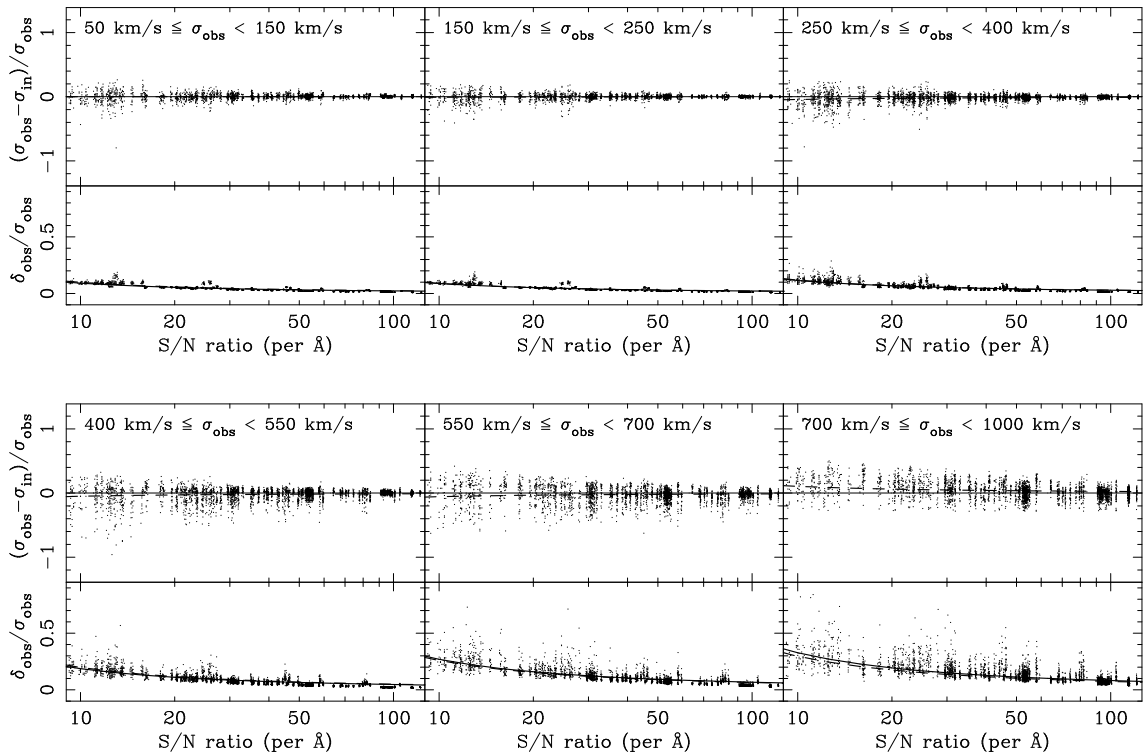


FIG. 9.— Monte Carlo simulations with more than 3×10^4 realizations of our NGC 6166 spectra for which (1) there is no mismatch between the template and the artificial galaxy spectra; and (2) surface brightness $I_{in} \geq 0.05 I_{sky}$. The upper panels show the true fractional errors in σ as a function of “observed” velocity dispersion, σ_{obs} . The “observed” parameters σ_{obs} and the formal errors, δ_{obs} , were derived by applying the direct fitting method of Kelson et al. (2000) to the simulated spectra. The velocity dispersions input into the simulated spectra are denoted by σ_{in} . Any systematic offsets between the points in the upper panels from zero would indicate a decrease in our ability to accurately measure velocity dispersions within a given range of σ_{obs} . The dashed lines in the upper panels show the systematic error in σ_{obs} as a function of S/N ratio. These diagrams indicate that our method can reliably recover velocity dispersions up to $\sigma_{obs} \lesssim 700$ km/s. For larger values of σ , there appear to be systematic errors $\gtrsim +5\%$ for $S/N \lesssim 30$ per \AA . The lower panels show the observed formal errors as a function of S/N ratio in the given velocity dispersion ranges. The mean formal error as a function of S/N is shown by the solid line while the “true” formal errors, as derived from the scatter in the upper diagrams, is shown by a dashed lines in each of the lower panels. The agreement between the two curves illustrates that our formal errors are reliable estimates of the random error in the measurement.

radial bin, in kpc; (2) the length of the radial bin, in kpc, (3) σ , the velocity dispersion, in km s^{-1} ; (4) δ_σ , the formal error in σ , in km s^{-1} ; (5) V , the mean line-of-sight radial velocity, in km s^{-1} ; (6) δ_V , the formal error in V , in km s^{-1} ; and (7) the reduced χ^2 of the fit.

5. MONTE CARLO SIMULATIONS OF THE ACCURACY OF VELOCITY DISPERSION MEASUREMENTS

Accurate measurement of velocity dispersions, *i.e.*, absorption line widths, from galaxy spectra requires: (1) that the instrumental broadening of the galaxy spectrum must be (approximately) less than the intrinsic Doppler broadening; and (2) that there must be statistically significant structure on scales comparable to the Doppler broadening. If either of these requirements is not satisfied, systematic errors may become important. The great difficulty in measuring the velocity dispersion profiles of galaxies to large radii, and for cD galaxies in particular, is that this last requirement may not be satisfied at large projected radii. In the cD halo, the potential may become dominated by dark matter and the stars may have similar kinematics to the cluster galaxies. Furthermore, the surface brightness of the stellar component of the cD halo is typically quite low (several magnitudes below the dark sky in the B -band). At such low surface brightnesses even a small error in the background subtraction can introduce unwanted

structure/power into the extracted galaxy spectrum. Because the representative sky spectrum in Figure 5 has significant power on the scales relevant for the measurement of absorption line velocity widths, there exist the possibilities of over-estimated S/N ratios and of excess structure in the spectra at a sufficient level to bias the deduced LOSVD. In this section we analyze simulations of our data to determine under what conditions such systematic effects become important and at what level our measurements of the kinematics in NGC 6166 may no longer be trustworthy.

Because our data span a wide range of measured velocity dispersions over a broad range of surface brightnesses, we constructed 4680 artificial galaxy spectra with intrinsic broadening of $\sigma_{in} \in \{100, 200, 300, 400, 500, 600, 700, 800, 900\}$ km/s. We used the 10 Gyr-old, solar metallicity, blue SED from Vazdekis (1999) as the underlying spectrum of the artificial galaxy. These spectra reproduce the characteristics of the NGC 6166 data, assuming a range of surface brightnesses, $I_{in} \in \{3.0, 1.0, 0.5, 0.1, 0.05\} \times I_{sky}$, and sky subtraction errors, $E_{in} \in \{\pm 0.02, \pm 0.01, \pm 0.005, \pm 0.001, 0.0\} \times I_{sky}$. The artificial spectra were given a range of S/N ratios equivalent to summing several CCD rows as in §2.2.3 ($10 \leq N_{rows} \leq 1000$, depending on the desired S/N ratios).

With the many variations described in the previous paragraph, 3×10^4 artificial spectra were created with

$5 \lesssim S/N \lesssim 200$ per Å. The key results of fitting these simulated galaxy spectra with a perfect template are shown in Figure 9. In the upper panels, for several ranges of “observed” velocity dispersions (σ_{obs}), we show the fractional error in σ , $(\sigma_{obs} - \sigma_{in})/\sigma_{obs}$, as a function of S/N ratio. If the data points cluster about the solid lines, then our methods are free from any systematic errors (template mismatch is not explored in this figure). The dashed lines show the best-fit curve of $(\sigma_{obs} - \sigma_{in})/\sigma_{obs} \propto [\log(S/N)]^{-2}$. For $\sigma_{obs} \lesssim 700$ km/s, the measured velocity dispersions are free from systematic errors for $S/N \gtrsim 10$ per Å. Figure 9 suggests the presence of systematic errors when $\sigma_{obs} \gtrsim 700$ km/s and $S/N \lesssim 30$ per Å, but this is an artifact of the restriction $\sigma_{in} \leq 900$ km/s (in other words, $\sigma_{obs} = 800$ km/s with an error of -20% does not appear because there were no artificial spectra with $\sigma_{in} = 960$ km/s). Based on the upper panels we conclude that the velocity dispersion profile derived in §4 is free from systematic errors (other than template mismatch, discussed below).

The lower panels of Figure 9 show the formal errors, δ_{obs} , in σ_{obs} as a function of S/N ratio. The solid lines show the best-fit functions of the form $\delta_{obs}/\sigma_{obs} \propto [\log(S/N)]^{-2}$ and illustrate the correlation of the estimated formal errors in σ with S/N ratio. These estimates for the formal errors can be empirically verified using the scatter in the upper diagrams. The best-fit functions (using the same form), which represent the correlations of the true random errors with S/N ratio, are shown by the dashed lines in the lower panels. The agreement between the two curves is excellent and indicates that we have satisfactorily estimated the random errors in σ .

The simulations were also used to explore whether fitting the Ca H & K features improves one’s ability to resolve large values of the Doppler broadening. The 4000Å break and the H & K lines are broad features with presumably sufficient power on the scales required to accurately measure large velocity dispersions ($\sigma \gtrsim 500$ km/s). However, incorporating that region of the spectrum does not improve the measurement of σ because the S/N ratios are much lower than those in the region around the G band, a more useful feature because of the confluence of the higher fluxes and the intrinsic 2000 km/s width of the feature.

We also used the simulations to explore the effects of template mismatch. By fitting the artificial galaxy spectra with spectra of individual late-type stars, we found small systematic errors on the order of $\lesssim 5\%$. These systematic errors are not correlated with S/N ratio, and if one adopts the template that produces the lowest χ^2 , the error is minimized. Such systematic uncertainties, at a level of a few percent, are likely to be present in our velocity dispersion profile for NGC 6166.

The simulations shown in Figure 9 also point to an additional effect that will impact future studies: for a given desired fractional error in σ , large velocity dispersions require data with higher S/N ratios. For example, measuring an internal velocity dispersion of $\sigma = 900$ km/s with an accuracy of $\pm 10\%$ requires spectra with $S/N = 50$ per Å. An accuracy of $\pm 15\%$ requires $S/N = 30$ per Å. Fortunately we did not find such large velocity dispersions in §4, even at a projected radius of 60 kpc. In the future, however, when

the observer pushes towards larger radii and/or lower surface brightnesses in other targets, such levels of Doppler broadening may occur, and acquiring data with such high S/N ratios will be necessary to produce credible measurements of the internal kinematics. This requirement may be difficult to meet with current 8m-10m telescopes (even using the sky-subtraction technique of (Sembach & Tonry 1996)).

In summary we conclude that the velocity dispersion profile derived in §4 is free from systematic errors at the level of $\pm 3\%$. Most of the systematic error arises from a mismatch of the template star with the galaxy.

6. SIMPLE SPHERICALLY SYMMETRIC MODELS

Under dynamical equilibrium, the observed velocity dispersion profile is a constraint on the density profile (Jeans 1915). In principle one can invert the observed kinematics to directly infer the underlying distribution of mass (Binney & Mamon 1982) or use orbital-superposition approaches to build realistic mass models (Schwarzschild 1979; Richstone & Tremaine 1984; Rix et al. 1997). However, the construction of anisotropic mass models requires measurements of the Gauss-Hermite moments h_3 and h_4 , and we did not achieve sufficiently high S/N ratios to measure these higher order moments of the LOSVD in the outer parts of NGC 6166 ($\gtrsim 40$ per Å is required; van der Marel & Franx 1993), and our measurements in the inner parts were corrupted by the interloper (§4).

With kinematics from only one position angle, and without the high-order moments of the LOSVD, several assumptions must be made before deriving meaningful constraints on the mass profile. For the modeling of NGC 6166 and Abell 2199, we assume spherical symmetry and zero net rotation. Even though the isophotes of NGC 6166 have ellipticities ranging from 25% at $R = 5$ kpc to to 50% at $R = 75$ kpc (Fig. 8, and the cD halo appears to be rotationally flattened, this rotation accounts for less than $\lesssim 5\%$ of the kinetic energy in the cD halo. Because neither the bulk of the cD, nor the cluster member kinematics, is supported by rotation, the mild rotation in the outskirts of the cD has little impact on the modeling. We also note that the ellipticity of the isophotes does not necessarily invalidate our assumption of spherical symmetry — the total gravitational potential is most likely close to spherical given the morphology of the cluster.

Thus this section is devoted to fitting simple spherically symmetric 1- and 2-component mass models to the velocity dispersion profile of NGC 6166. The reduction of the Jeans equations to spherically symmetry greatly simplifies the computation of the projected line-of-sight velocity dispersion profiles, $\sigma(R)$, for the model mass profiles we explore below.

For non-rotating spherical systems the Jean’s equations (Equations 4-55, 4-57a, and 4-60 of (Binney & Tremaine 1987) are:⁸

$$\frac{GM(r)}{r} = -\overline{v_r^2} \left(\frac{d \ln \nu}{d \ln r} + \frac{d \ln \overline{v_r^2}}{d \ln r} + 2\beta(r) \right) \quad (5)$$

$$I(R) = 2 \int_R^\infty \frac{\nu r dr}{\sqrt{r^2 - R^2}} \quad (6)$$

⁸ The integrals are evaluated numerically using the ODEPACK and QUADPACK (<http://www.netlib.org/>) routines from within Python (<http://www.python.org/>) scripts.

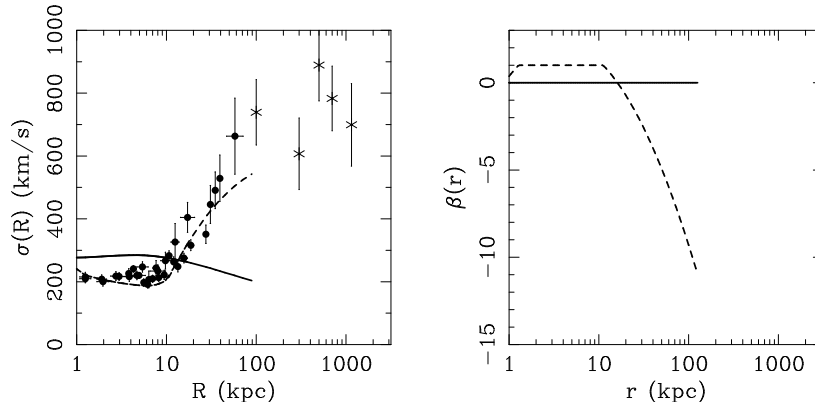


FIG. 10.— The observed velocity dispersion profile of NGC 6166 and its halo from integrated starlight (filled circles) and Abell 2199 from cluster member kinematics (crosses). The solid line is the projected line-of-sight velocity dispersion profile of the best-fit isotropic single-component stellar mass model in which a power-law stellar density profile is used. The dashed line illustrates that the rising velocity dispersion profile of NGC 6166 can be well fit by an anisotropic model, while the right-hand panel shows the anisotropy used in the two models. Such high levels of anisotropy are not seen in other giant ellipticals and BCGs (typically $-0.5 \lesssim \beta \lesssim 0.5$; Saglia, Kronawitter, Gerhard, & Bender 2000; Kronawitter et al. 2000; Gerhard et al. 2001), and result in mass models that cannot support the velocity dispersion of the cluster unless the galaxies also follow such strongly tangentially anisotropic orbits.

$$I(R)\sigma^2(R) = 2 \int_R^\infty (1 - \beta(r)) \frac{R^2}{r^2} \frac{\nu \overline{v_r^2} r dr}{\sqrt{r^2 - R^2}}, \quad (7)$$

where $\beta(r) \equiv 1 - \overline{v_\theta^2}/\overline{v_r^2}$, ν is the stellar density at r as constrained by the surface photometry, and $M(r)$ is the total gravitational mass enclosed within radius r . The gravitational mass, $M(r)$, includes the stellar mass and relies on assumptions about the radial gradient in the stellar M/L ratio. With the radial gradients in M/L_B suggested in §3, the stellar density decreases more quickly than in the case of constant M/L_B . However, in the case of a decreasing M/L_B gradient, the light-weighted integrals in Equations 6 and 7 are weighted towards larger radii, where the stars are increasingly more luminous per unit mass.

For each parameterized model, we perform a search for the parameters that minimize the square of the residuals between the model and observed velocity dispersion profiles. We choose to uniformly weight the data because weighting by the inverse of the formal errors would cause the minimization algorithm to find the parameters that best fit the inner regions of the galaxy. Furthermore, we exclude the inner $R = 2'' \equiv 1.1$ kpc from the fit because: (1) this region is heavily affected by the seeing (recall: $0''.8$ FWHM); and (2) the spectrum in the center shows evidence for nuclear activity (also noted by Fisher, Illingworth, & Franx 1995) and it is likely that a massive black hole dominates the kinematics in the very center, given the correlation between galaxy and central black hole masses (Gebhardt et al. 2000).

Given the simplicity of the models, we attempt no derivation of uncertainties in the parameters of each model as their meaning could only be as valid as any given model is an appropriate representation of the mass distribution, or as valid as any of the underlying assumptions. Instead we use the χ^2 minima to assess whether given mass models are consistent with the data at a given confidence level ($\geq 95\%$).

6.1. Single-Component Mass Models

In this section we fit the data with models containing a single mass component. Two single-component mass mod-

els are considered here: (1) a distribution of stars alone; and (2) a distribution of dark matter alone, in which the stars are effectively massless tracers of the dark potential (the stellar M/L is identically zero). While fitting single-component mass models is unlikely to provide physically meaningful characterizations of the distribution of mass in the core of Abell 2199 given the presence of both stars and dark matter, these models provide natural starting points for illustrating to what extent additional components might be required. After a brief discussion of the deficiencies of the single-component models, two-component mass models will be discussed in §6.2

6.1.1. Single Component Stellar Model

For this exercise, the observed velocity dispersion profile of NGC 6166 is fit using a mass density model defined by the fit of a King (1966) model to the surface brightness profile (see §3, under the assumption of a constant M/L_* ratio). The structural parameters for this model are listed in Table 1, leaving the overall normalization of M/L_* and the anisotropy as the only free parameters. For this model we explore two variants: the isotropic case and the case in which the anisotropy, $\beta(r)$, has been adjusted to provide a reasonable match to the dispersion profile.

We show these models in Figure 10(a), using the solid line to denote the best-fit isotropic model and the dashed line to illustrate the best-fit anisotropic model. Figure 10(b) shows the anisotropy required to reproduce the observed velocity dispersion profile. These models illustrate that the stellar mass alone cannot support the rising $\sigma(R)$ profile in the cD halo, unless the stellar orbits become significantly (and unreasonably) tangentially anisotropic (also see Tonry 1983). Such levels of anisotropy are inconsistent with what has been observed at $1-2 r_e$ in other brightest cluster galaxies (typically $-0.5 \lesssim \beta \lesssim 0.5$; Saglia, Kronawitter, Gerhard, & Bender 2000; Kronawitter et al. 2000; Gerhard et al. 2001).

The purely stellar models imply a total mass of $M_* = 4 \times 10^{12} M_\odot$. This mass is insufficient to support the observed velocity dispersion of the cluster galaxies $\sigma_{A2199} =$

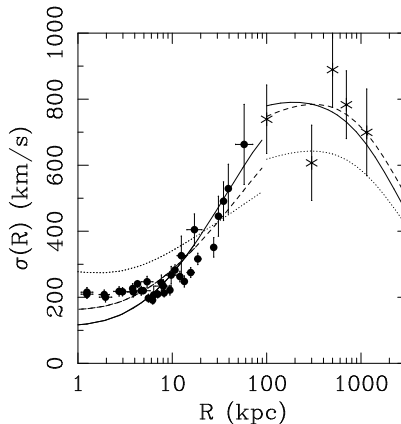


FIG. 11.— The observed velocity dispersion of NGC 6166 and its halo from integrated starlight (filled circles) and Abell 2199 from cluster member kinematics (crosses) as a function of projected radius with the single-component dark matter models overlaid. The solid, dashed, and dotted lines show the best-fit $\alpha = 0, 1, 1.5$ generalized-NFW density profiles, respectively.

$775 \pm 50 \text{ km s}^{-1}$, unless the galaxy kinematics become even more strongly tangentially anisotropic (essentially following an extrapolation of the dashed line in the figure). Figure 10(a) shows the velocity dispersion profile of the cluster derived from the 127 member galaxies within $R \leq 1.5$ Mpc (obtained from NED). Given that the orbits of cluster galaxies are typically close to isotropic (Natarajan & Kneib 1996; van der Marel et al. 2000), it is unlikely that the galaxy orbits in Abell 2199 are as anisotropic as would be required with the purely stellar mass model. Even if M/L_* is not a constant, under the constraints of §3, $M(R)$ converges even more rapidly. As a result, the outskirts of NGC 6166 would be required to be more strongly anisotropic than in the case of a constant M/L_* .

We consider the single-component stellar models unfeasible because both the stellar and galactic orbits are required to be unreasonably tangentially anisotropic in order to support the large observed velocity dispersions.

6.1.2. Single Component Dark Matter Model

We now model the data using a single-component dark mass profile, in which the stars of NGC 6166 are massless tracers of the potential. In order to compute the projected line-of-sight velocity dispersion profile for NGC 6166, we use the stellar luminosity density profile (the projected velocity dispersion for the galaxy is a *light*-weighted moment of the LOSVD). At larger radii, where the kinematics of cluster galaxies are sampled, we assume that the galaxy number density traces the density of the dark matter model. This assumption is valid because van der Marel et al. (2000) found that galaxy number density profiles of the CNOC1 clusters traced the mean dark matter density profile well.

In Figure 11 we show the best-fit models using generalized-NFW density profiles with $\alpha \in \{0, 1, 1.5\}$. Because the NGC 6166 data-points have smaller relative uncertainties, the cD data carry more weight than the cluster data, and the extremely cuspy $\alpha = 1.5$ model simply cannot be adjusted to fit both the inner regions of the cD while maintaining the overall normalization of the total mass as constrained by the cluster data. Even for the softer halos, a single component model cannot fit the galaxy and the cluster velocity dispersion profile simultaneously. The soft $\alpha \leq 1$ model fits the rise in $\sigma(R)$ and the cluster data

quite well, but leaves a hole in the inner region where the non-zero stellar mass of the cD resides.

The concentration parameter, $c = R_{200}/r_s$, is left as a free parameter in the fit. The best-fit $\alpha = 1$ profile has $c = 4$ and $R_{200} = 1.6$ Mpc. Bullock et al. (2001) discussed the scatter in concentration parameters as a function of halo mass, and while they do not address halos as massive as ours ($M_{200} = 5 \times 10^{14} M_\odot$), an extrapolation of their Figure 4 indicates that $c = 4$ would fall within the $\pm 1\sigma$ range of concentration parameters at this halo mass.

Figure 11 also illustrates an important physical effect in the mass modeling: that if the density profile of the cD halo does not trace the number density profile of the galaxies in the cluster, then the velocity dispersion profiles of the two components will not be identical at a given projected radius. (also see Natarajan & Kneib 1996). This effect appears as a discontinuity between the model velocity dispersion profiles of the cD and the cluster. As the minimization algorithm adjusts the shape of the dark matter density profile, the inferred number density profile of cluster galaxies may not have the same shape as the stellar density profile in the outskirts of the cD. As a result, the best-fit dark matter model may imply a distribution of galaxies that traces the potential differently than the stars in cD halo do (at a fixed projected radius). This difference results in a velocity dispersion profile for the cD that may not seamlessly join the velocity dispersion profile of the cluster. Under different assumptions (forcing the stars in the cD halo to have originated from the current distribution of cluster galaxies), the velocity dispersion profiles of the cD and the cluster can be made a single, continuous function. Perhaps a future analysis of the color and absorption line strength gradients will help to constrain nature of the relationship between the stars in the cD halo and the cluster galaxies.

In this section we restricted ourselves to isotropic dark matter models, a reasonable assumption because the CNOC1 clusters appear to be isotropic (van der Marel et al. 2000), and also because X-ray observations of Abell 2199 constrain the anisotropy in the dark matter velocity distributions to $-0.5 \lesssim \beta \lesssim 0.5$ over a wide range of cluster radii (Mahdavi 2001). The conclusions drawn from the models in this section are insensitive to these levels of

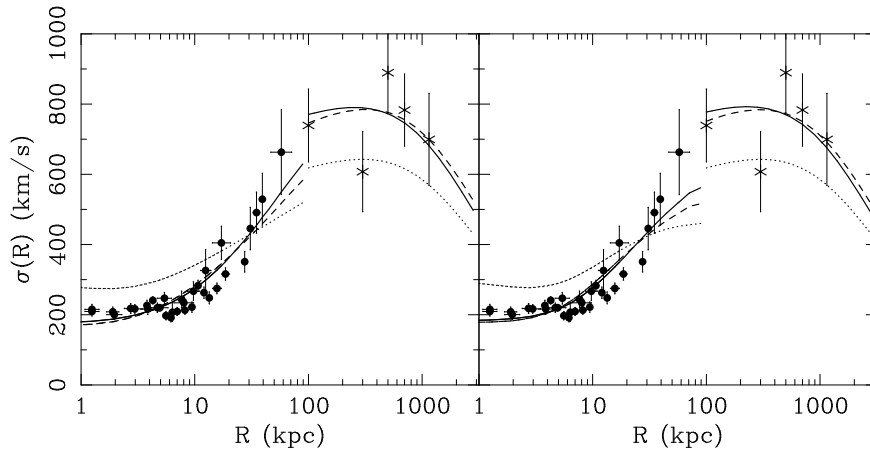


FIG. 12.— The observed velocity dispersion of NGC 6166 and its halo from integrated starlight (filled circles) and Abell 2199 from cluster member kinematics (crosses) as a function of projected radius, with simple two-component models overlaid in which (a) a power-law density profile or (b) King (1966) model is used to represent the stellar mass. These models assume a constant B -band stellar M/L_* ratio and the solid, dashed, and dotted lines indicate the models with the generalized-NFW dark matter halos for which $\alpha = 0, 1, 1.5$, respectively. The models with $\alpha = 0$ have stellar M/L ratios $M/L_B = 9$, consistent with the M/L_* ratios seen in other giant ellipticals (Gerhard et al. 2001). With $\alpha = 1$, $M/L_B = 1.2$ and 0.2 when the two stellar mass density profiles are used, respectively. Using $\alpha = 1.5$ forces $M/L_B = 0$, and these models still have far too much dark matter in the core to adequately match the observed velocity dispersion profile.

anisotropy.

6.2. Two-Component Mass Models: Stars + Dark Matter

The previous section showed that one-component isotropic mass models do not satisfactorily reproduce the projected line-of-sight velocity dispersion profile of NGC 6166. With this discrepancy in mind, we take the dark models and add a component that physically represents the stellar mass of the cD. The stellar mass profile is directly constrained by the surface photometry, with the overall normalization (the stellar M/L ratio) to be constrained by $\sigma(R)$ in the inner regions of the galaxy.

In this section we find the best-fit two-component isotropic mass models (see earlier references to Saglia, Kronawitter, Gerhard, & Bender 2000; Kronawitter et al. 2000; van der Marel et al. 2000; Mahdavi 2001, regarding isotropy). The two mass components are expected to represent the stellar mass of the cD and the dark matter distribution of the cluster. Because the surface brightness profiles of giant ellipticals are well-fit by power-law and King (1966) density models (King 1978; Lauer 1985; Graham et al. 1996), we explore models in which the stellar component is modeled either by a power-law mass density profile or by a King model density profile, with structural parameters given in Table 1. The dark matter distribution of the cluster is parameterized by the generalized-NFW halo profile.

In Figure 12(a), we show the best-fit models for the case where a power-law density profile of constant M/L_* ratio is used to parameterize the stellar mass of the cD and where generalized-NFW density profiles with $\alpha \in \{0, 1, 1.5\}$ are used to parameterize the dark matter halo. Figure 12(b) uses a King (1966) model for the stellar mass profile, and the dark matter halo density profiles are parameterized as in 12(a). When fitting models with an $\alpha = 1$ halo, we find concentration parameters of $c = 3.5$ and 4.5 depending on whether the stellar mass is modeled as a power-law or King model, respectively. As above, these c values are consistent with the $\pm 1\sigma$ range for the concentration given by Bullock et al. (2001).

Of these two-component models, the dark matter halo profiles with $\alpha = 0$ fit best, yielding a B -band M/L_* ratio of $M/L_B = 9$ for either parameterization of the stellar density profile. If $\alpha = 1$, the power-law density and King parameterizations have $M/L_B = 1.2$ and 0.2 , respectively. Using a dark matter halo with $\alpha = 1.5$ cannot reproduce the observed velocity dispersion profile because the halo density profile has too much dark matter in the core (thus forcing $M/L_* = 0$). The stellar M/L_B ratio derived using $\alpha = 0$ is consistent with what has been derived for other giant ellipticals and BCGs ($8 \lesssim M/L_B \lesssim 12$ for $M \gtrsim 10^{11} M_\odot$; Gerhard et al. 2001). The $\alpha = 1$ model is unlikely because the deduced M/L_B is inconsistent with the $B - R$ color of the galaxy (for realistic initial mass functions, an extrapolation of the (Vazdekis et al. 1996) models to $M/L_B = 1$ and $B - R = 1.5$ implies a mean stellar population age of 24 Myr and $[\text{Fe}/\text{H}] = +2.4$).

Allowing for the gradient in M/L_B , as constrained in §3, does not solve the problem. As stated earlier, the color gradient implies that $M(R)$ converges rapidly for the stellar component. While the implication is that there is less stellar mass at large radii, the normalization of the stellar mass density profile is determined by the velocity dispersions within $R \lesssim 10$ kpc. Together these effects produce a deficiency of stars at large radii, but there is no net impact on the model velocity dispersion profiles because the dark matter halo is adjusted during the χ^2 minimization to maintain the total mass profile of the system. Furthermore, if the stellar mass profile converges very rapidly, as is the case where the color gradient arises from a gradient in the mean stellar population ages, more dark matter is required to support the motions of the stars in the outskirts of the galaxy. This need for additional dark matter at such radii is found by shrinking the core radius of the dark matter halo, but not by making the core cuspiest (see earlier discussion). As a consequence, our conclusions are actually insensitive to the assumption of a constant M/L_* ratio. Only in systems without a massive, compensating component of dark matter at large radii, will the gradi-

ent in stellar populations have a significant impact on the inferred total mass profile.

6.3. Additional Points

There are some additional limits to our data that should be noted. For example, the two-component mass models that employ the power-law density profile for the stellar mass produce a steeper $\sigma(R)$ gradient beyond $R = 20$ kpc than the equivalent models that use King stellar mass profiles. This difference arises because the power-law density profile has infinite extent, with the density falling as $\rho \propto r^{2.5-3}$, and the King model has finite extent. The surface photometry is not well-fit by an isothermal sphere and, as a result, the King model fit is truncated at a finite radius. In the integration to large radii there will simply be more light at larger radii with a power-law stellar density profile and thus a steeper gradient in $\sigma(R)$.

We also investigated whether a King model was a better parameterization for dark matter density profile. Both the King model and $\alpha = 0$ generalized-NFW halo have similarly shaped density profiles in the inner regions, but they transition, respectively, to $\rho \propto r^{-2}$ and $\rho \propto r^{-3}$ at large radii. Unfortunately the current data do not extend beyond 1.5 Mpc, and we are therefore unable to determine whether the density profile of the dark matter halo declines either as $\rho \propto r^{-2}$ or as $\rho \propto r^{-3}$. A better determination of the cluster density profile at large radii awaits membership surveys that extend beyond R_{200} (e.g., as in Rines et al. 2000). Such data would not only provide greater leverage on the shape of the mass profile at large cluster radii, but such membership information would allow for a test of the assumption that the galaxy number density traces the dark matter density.

6.4. Comparison with X-Ray Masses

At large radii, the inferred mass of the system is insensitive to the model adopted for the stellar density profile and mildly sensitive to the adopted dark matter density profile. With the $\alpha = 0$ generalized-NFW halo, we obtain $M(< 0.5h^{-1} \text{ Mpc}) = 1.7 \times 10^{14}h^{-1}M_{\odot}$ ($h = H_0/100$) when adopting either the power-law or King model stellar density profile (and $M(< 0.5h^{-1} \text{ Mpc}) = 1.5 \times 10^{14}h^{-1}M_{\odot}$ with $\alpha = 1$). These mass estimates are consistent with the mass derived from ASCA and ROSAT X-ray data: $M(< 0.5h^{-1} \text{ Mpc}) = (1.45 \pm 0.15) \times 10^{14}h^{-1}M_{\odot}$ (Markevitch et al. 1999).

For radii within $\sim 0.1h^{-1} \text{ Mpc}$, most X-ray mass determinations have been hampered by the relatively poor spatial resolution of the instruments and by what may be a central cooling flow (Siddiqui, Stewart, & Johnstone 1998; Markevitch et al. 1999). As a result, there has been some variation in the published mass estimates: Markevitch et al. found $M(< 0.1h^{-1} \text{ Mpc}) = (0.33 \pm 0.06) \times 10^{14}h^{-1}M_{\odot}$, whereas Siddiqui et al. (1998), who use only the ROSAT PSPC data, found $M(< 0.1h^{-1} \text{ Mpc}) \approx 0.22 \times 10^{14}h^{-1}M_{\odot}$ (from their Figure 15). The difference between Markevitch et al. and Siddiqui et al. stems from the need to extrapolate the mass profile into the region of the cooling flow: Markevitch et al. (1999) modeled the X-ray temperature profile of the cluster using a polytrope and Siddiqui et al. (1998) modeled the cluster using a King profile. Because polytropes are, by definition, cus-

pier than the isothermal cores of King models, Siddiqui et al. (1998) infer a shallower mass profile. Using X-ray data from Chandra, with much higher spatial and spectral resolution, Johnstone et al. (2002) suggest that the NFW profile provides a marginally better description of the *total* gravitational mass profile than $\alpha = 1.5$ or a non-singular isothermal sphere (also see §6.1.2). Using their best-fit NFW model, those authors infer $M(< 0.1h^{-1} \text{ Mpc}) \approx 0.15 \times 10^{14}h^{-1}M_{\odot}$. Despite the uncertainties in the X-ray mass determinations, their estimates are in reasonable agreement with the values yielded by our two-component models: $M(< 0.1h^{-1} \text{ Mpc}) = 0.17 - 0.19 \times 10^{14}h^{-1}M_{\odot}$.

6.5. Reconciling Soft Halo Profiles with Strong Gravitational Lensing

Given its low redshift, there are currently no gravitational lensing data for Abell 2199. However, it is possible to ask whether the strong lensing characteristics of our two-component mass models are consistent with the properties of known strong lenses at intermediate redshifts. Figure 13 shows a plot of the tangential critical radii of our two-component mass models when placed at the redshifts $z_{lens} \in \{0.2, 0.3, 0.4, 0.5\}$. We restrict the figure to only include the two-component models with dark matter halo density profiles with $\alpha = 0$ and 1, because these models are able to reproduce the internal kinematics of NGC 6166 and the surrounding cluster. We mark the radii for tangential arcs in several intermediate redshift clusters, using crosses when the source redshift is known, and horizontal dotted lines when the source redshift is unknown. The horizontal shaded bar marks the *R*-band effective radius (see Table 1 that NGC 6166 would have at z_{lens} . At $z_{lens} = 0.2$, the strong lensing would be difficult to observe because the resulting arcs would be deep inside the image of the cD. Beyond $z_{lens} \gtrsim 0.3$, the tangential critical radii lie well outside r_e and any strong lensing would be observable. The radii of arcs in clusters at $z_{lens} \gtrsim 0.3$ are in rough concordance with our model predictions.

As an additional note, the model with an $\alpha = 0$ NFW halo yields larger critical radii than the $\alpha = 1$ NFW halo. This effect occurs because a more massive central galaxy is needed to reproduce the observed velocity dispersions within the central 10 kpc, and this extra structure in the mass profile gives the lensing signal a boost. While the current modeling has neglected departures from spherical symmetry and substructure, such effects serve to increase the predicted critical radii and improve the agreement (Bartelmann et al. 1995). Furthermore, if the dark matter halo density profile transitions at large radii to $\rho \sim r^{-2}$ instead of $\rho \sim r^{-3}$, the excess surface mass densities can increase the predicted critical radii by factors of a few.

In Figure 13, the predicted critical radii increase with z_{lens} for a given z_{source} . However, there appears to be no significant correlation of the observed arc radii with z_{lens} . The natural distribution of θ_{crit} may not be as narrow as indicated by the observed arc radii, but may be truncated at low θ_{crit} by the presence of large brightest cluster galaxies and by the limited spatial resolution of ground based imaging. These effects are likely to be the cause of the poor agreement between the predicted critical radii of our mass models at $z_{lens} = 0.2$ and the arc radii seen in $z \approx 0.2$ clusters.

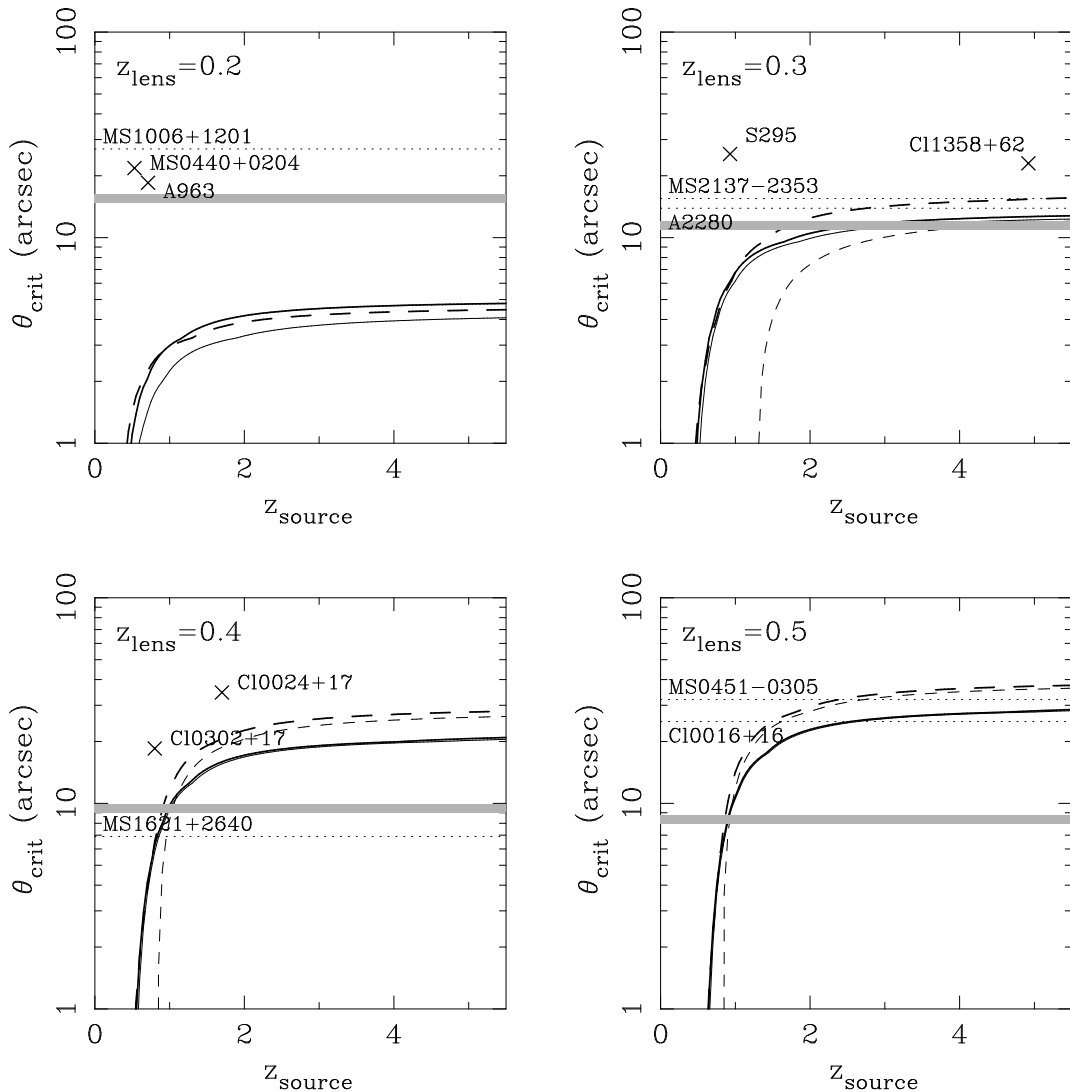


FIG. 13.— The projected radii for the tangential critical curves as a function of source redshift for several possible lens redshifts for our two-component mass models. We show the best-fit two-component mass models in which the stellar density profile is parameterized by a power-law and the dark matter halo is parameterized either by $\alpha = 0$ (thick dashed) or by $\alpha = 1$ (thick solid). The thin dashed and thin solid lines show the critical radii derived from the dark matter halos of those two-component models alone, ignoring the mass of the cD. Using the compilation of tangential arcs in Williams et al. (1999), we show example arcs seen in intermediate redshift clusters, using crosses when the source redshift is known and horizontal dotted lines when the source redshift is unknown. The horizontal gray bars indicate the effective radius NGC 6166 would have at each z_{lens} . If Abell 2199 were redshifted to cosmological distances, the cluster’s mass profile would produce arcs similar to those seen in intermediate redshift clusters. For the case of the $\alpha = 0$ dark matter halo, the stellar mass serves as a large boost to the lensing signal. In the two-component mass model with $\alpha = 1$, the stellar mass-to-light ratio is too low for the addition of the stellar mass to significantly affect the critical radii. Note that at $z_{lens} = 0.2$, the surface brightness of the cD would likely mask any strong arcs. Furthermore, because the greatest probability for lensing occurs when $z_{source} = 2z_{lens}$, the predicted θ_{crit} would also be difficult to observe with the limited spatial resolution of ground-based imaging.

The strong gravitational lensing by MS2137–2353 has been used to constrain the mass profile of the cluster (Miralda-Escudé 1995), and to predict a rising line-of-sight velocity dispersion profile for the central galaxy. The predicted velocity dispersion profile for the central galaxy of MS2137–2353 is similar to the velocity dispersion profile of NGC 6166, and in modeling the lensing cluster, Miralda-Escudé (1995) also ruled out dark matter density profiles with $\rho \propto r^{-1}$ in the inner region of the cluster.

To summarize the mass profile we derived reproduces our observation of the kinematics in NGC 6166 and the surrounding cluster and is also consistent with the X-ray mass determinations for Abell 2199 and with observations of strong lensing in intermediate redshift clusters.

7. DISCUSSION

The cD galaxy NGC 6166 clearly shows a rise in σ with projected radius, nearly reaching the observed velocity dispersion of the galaxies in the surrounding cluster. NGC 6166 is only the second cD galaxy with a measured velocity dispersion profile that rises at large radii, after IC 1101 (Dressler 1979). A rising velocity dispersion profile is not seen in the simulation by Dubinski (1998), in which he constructs a cD-like galaxy through the continuous accretion of rotationally-supported spiral-like galaxies.

The soft ($\alpha < 1$) uniform density core of NGC 6166’s dark halo is also inconsistent with cosmological N -body simulations with inert CDM (Davé et al. 2001). Many

authors have now begun to explore other forms of cold dark matter, such as self-interacting, warm, or differently mutated forms of dark matter (Spergel & Steinhardt 2000; Yoshida et al. 2000; Davé et al. 2001; Colín et al. 2000; Dalcanton & Hogan 2001). The most extreme cases of active dark matter produce flat ($\alpha = 0$) halo cores, but some fine-tuning of the dark matter interaction cross section may be required to avoid creating a universe of perfectly spherical halos (Miralda-Escudé 2002). Perhaps the discrepancy will be resolved with α being a function of scale (Jing & Suto 2000); though see (Klypin et al. 2001).

For the moment, the simulations are difficult to interpret. Not only is the scatter in α poorly known, but the quoted values of α have been derived by fitting the halo profiles outside $r \gtrsim 0.03R_{200}$ ⁹ (Klypin et al. 2001), and the consequences of the implied extrapolation of the parameterized models to $r \rightarrow 0$ are ignored. Taylor & Navarro (2001) argue that the phase-space density profiles of dark matter halos are well-approximated by power-laws over $0.01R_{200} \lesssim r \lesssim R_{200}$, and those authors extrapolate the power-law phase-space density profile to $r = 0$ to obtain $\alpha = 0.75$ (for NGC 6166 $\alpha = 0.75$ implies $M/L_B = 4.5$, too low by a factor of two, Gerhard et al. 2001). Including the effects of baryons will likely be important on these scales as the cooling of baryonic matter will result in adiabatic contraction (Blumenthal, Faber, Flores, & Primack 1986; Rix et al. 1997; Keeton 2001), which steepens the inner profile of the halo (Alvarez, Shapiro, & Martel 2001). It has also been suggested that the transfer of angular momentum from the baryons to the dark matter can soften the cores of halos (Weinberg & Katz 2001; Klypin, Zhao, & Somerville 2002). Furthermore, Weinberg (2001) suggests a number of dynamical processes that can drive the cores of dark matter halos towards $\alpha \approx 0$.

Future simulations will hopefully resolve these problems either (1) by using more physically motivated boundary conditions in the extrapolation to $r \rightarrow 0$ (cf. Taylor & Navarro 2001), or (2) by resolving the physics within $r \lesssim 3\%R_{200}$. Because Weinberg (2001) and Nusser & Sheth (1999) suggest that the inner profiles of dark matter halos may be sensitive to their initial conditions and histories of collapse and merging, the simulations should ultimately (1) predict the cosmic scatter in α (at a given halo mass), and (2) provide the means to estimate the timescales of formation for dark matter halos of a given mass and α (instead of using the concentration parameter; Bullock et al. 2001).

8. CONCLUSIONS

We use the stellar kinematics of NGC 6166 and its halo to probe the mass distribution in the core of the rich cluster Abell 2199. The projected velocity dispersion along the major-axis of NGC 6166 rises steeply with radius beyond the projected radius $R \approx 10$ kpc (where $\mu_B \approx 23$ mag/arcsec²). The velocity dispersion profile decreases from about 300 km s^{-1} at $R = 0$ kpc to 200 km s^{-1} at $R = 2$ kpc (recall, the seeing was $0''.8$ FWHM $\equiv 0.45$ kpc), remains flat to $R \approx 10$ kpc, and then steadily rises to $660 \pm 120 \text{ km s}^{-1}$ at $R \approx 60$ kpc (where $\mu_B \approx 26$ mag/arcsec²), nearly reaching the velocity dispersion of

the cluster ($\sigma_{A2199} = 775 \pm 50 \text{ km s}^{-1}$). There is also evidence for mild rotation in intracluster stars beyond $R = 20$ kpc ($|V/\sigma| = 0.3$), which is not seen in the kinematics of the cluster members. Because we measure the velocity dispersion gradient with high precision, we have constrained the mass profiles of both the stellar and dark matter distributions, under the assumptions of isotropy and spherical symmetry.

The primary results of our work indicate that the gravitational potential of the cD halo is dominated by dark matter outside $R = 20$ kpc. Models in which the dark halo is represented by an $\alpha = 1.5$ generalized-NFW density profile (e.g., Moore et al. 1999) are not able to reproduce the observed dispersion profile. While the $\alpha = 1$ NFW profile is an improvement, the implied $M/L_B = 1$ is not consistent with what has been measured for other giant elliptical galaxies ($8 \lesssim M/L_B \lesssim 12$; Gerhard et al. 2001). In the models that utilize the $\alpha = 0$ generalized-NFW dark matter halo, one obtains $M/L_B = 9$, a more reasonable value.

The two-component mass models are consistent with the mass profiles derived from X-ray observations (Markevitch et al. 1999; Siddiqui, Stewart, & Johnstone 1998) over the range of radii for which our observations overlap. We also derived tangential critical radii for our two-component mass models assuming Abell 2199 were placed at cosmological redshifts. The predicted tangential critical radii are consistent with the radii of arcs in strong lensing clusters at intermediate redshift.

Our results obtained for Abell 2199 have strong implications for the study of dark matter halo profiles. The best-fit models are inconsistent with the predictions of N -body simulations of cold dark matter. However, we cannot yet verify the universality of dark matter halo profiles. Simulations are needed to provide more robust estimates of α at radii $r < 0.01r_{200}$ (see, e.g., Klypin et al. 2001) and to predict the scatter in α . Observationally, we are obtaining kinematical information for additional cD galaxies with the goal of providing empirical constraints on the scatter in dark matter halo properties.

With the possibility of observing cD galaxies to large radii using very long ($\gg 10'$) slits, the task of background subtraction will become easier and more accurate. Using a large database of cD galaxy kinematics, with several long-slit position angles per galaxy, we can explore more complicated models, in which both intrinsic flattening and anisotropy are included. At the same time, the expansion of catalogs of cluster galaxies (e.g., Rines et al. 2000), and dramatic increases in the spatial resolution of X-ray data, will enable us to better constrain the inner and outer slopes of dark matter halo profiles, while allowing us to avoid many of the simplifying assumptions. Such improvements may soon lead to the confirmation or refutation of universal dark matter density profiles, at least for the largest dynamically bound systems.

We would like to acknowledge helpful discussions with T. Lauer, D. Eisenstein, A. Dressler, and G. Evrard, R. Davé, F. van den Bosch, and to thank the entire staff of the W.M. Keck Observatory for their support. We also thank the anonymous referee for suggestions which

⁹ In our models $0.03R_{200} \approx 50$ kpc!

greatly improve the presentation of the material. AIZ acknowledges support from NASA grants NAG 5-11108 and HF-01087.01-96A. SCT acknowledges support from NASA grant HF-01125.01-99A and through grant NAS 5-26555. JSM acknowledges support from NASA grant NAG

5-3529. This research has made use of the NASA/IPAC Extragalactic Database (NED) which is operated by the Jet Propulsion Laboratory, California Institute of Technology, under contract with the National Aeronautics and Space Administration.

REFERENCES

- Alvarez, M., Shapiro, P. R., & Martel, H. 2001, *Revista Mexicana de Astronomia y Astrofisica Conference Series*, 10, 124
- Arabadjis, J.S., Bautz, M.W., & Garmire, G.P. 2001, *astro-ph/0109141*
- Bartelmann, M., Steinmetz, M., & Weiss, A. 1995, *A&A*, 297, 1
- Binney, J., & Mamon, G.A. 1982, *MNRAS*, 200, 361
- Binney, J., & Tremaine, S. 1987, *Galactic Dynamics*, Princeton University Press
- Blumenthal, G. R., Faber, S. M., Flores, R., & Primack, J. R. 1986, *ApJ*, 301, 27
- Bullock, J. S., Kolatt, T. S., Sigad, Y., Somerville, R. S., Kravtsov, A. V., Klypin, A. A., Primack, J. R., & Dekel, A. 2001, *MNRAS*, 321, 559
- Burstein D., & Heiles C. 1982, *AJ*, 87, 1165
- Carter, D., et al. 1985, *MNRAS*, 212, 471.
- Carter, D., Bridges, T. J., & Hau, G. K. T. 1999, *MNRAS*, 307, 131
- Cohen, J. & Ryzhov, A. 1997 *ApJ*, 486, 230.
- Colín, P., Avila-Reese, V., & Valenzuela, O. 2000, *ApJ*, 542, 622
- Côté, P., et al. 2001, *ApJ*, 559, 828
- Dalcanton, J.J. & Hogan, C.J. 2001, *ApJ*, 561, 35
- Davé, R., Spergel, D.N., Steinhardt, P.J., & Wandelt, B.D. 2001, *ApJ*, 547, 574
- Davies, R. L., Sadler, E. M., & Peletier, R. F. 1993, *MNRAS*, 262, 650
- Djorgovski S., & Davis M. 1987, *ApJ*, 313, 59
- Dressler, A. 1979, *ApJ*, 231, 659
- Dubinski, J. 1998, *ApJ*, 502, 141
- Faber S. M., Dressler A., Davies R. L., Burstein D., Lynden-Bell D., Terlevich R., & Wegner G. 1987, *Faber S. M., ed., Nearly Normal Galaxies*. Springer, New York, p. 175
- Firmani, C., D'Onghia, E., Chincarini, G., Hernández, X., & Avila-Reese, V. 2001, *MNRAS*, 321, 713
- Fisher, D., Illingworth, G.D., & Franx, M. *ApJ*, 438, 539
- Fisher, D., Franx, M., & Illingworth, G. 1996, *ApJ*, 459, 110
- Franx M., Illingworth, G.D., & Heckman, T. 1989, *AJ*, 98, 538
- Fukugita, M., Shimasaku, K., & Ichikawa T. 1995, *PASP*, 107, 945
- Gebhardt, K., et al. 2000, *ApJ*, 539, L13
- Gerhard, O., et al. 2001, *AJ*, 121, 1936
- Ghigna, S., et al. 2000, *ApJ*, 544, 616
- González, J.J. 1993, Ph.D. thesis, Univ. Calif., Santa Cruz
- Gorenstein, M.V., Falco, E.E., & Shapiro, I.I. 1988, *ApJ*, 327, 693
- Graham, A., Lauer, T.R., Colless, M., & Postman, M. 1996, *ApJ*, 465, 534
- Hammer, F., Gioia, I.M., Shaya, E.J., Teyssandier, P., Le Fèvre, O., & Luppino, G.A. 1997, *ApJ*, 491 477
- Hoekstra, H., Franx, M., Kuiken, K., & Squires, G. 1998, *ApJ*, 504, 636
- Iliev, I.T., & Shapiro, P.R. 2001, *MNRAS*, 325, 468
- Jeans, J.H. 1915, *MNRAS*, 76, 70
- Jing, Y.P., & Suto, Y. 2000, *ApJ*, 529, 69
- Johnstone, R. M., Allen, S. W., Fabian, A. C., & Sanders, J. S. 2002, 10 pages, 12 figures. Submitted to *MNRAS*, 2071
- Keeton, C. R. 2001, *ApJ*, 561, 46
- Kelson, D.D. 1998, Ph.D. thesis, Univ. of California, Santa Cruz
- Kelson, D.D., Illingworth, G.D., van Dokkum, P.G., & Franx, M. 2000, *ApJ*, 531, 159
- King, I.R. 1966, *AJ*, 71, 64
- King, I.R. 1978, *ApJ*, 222, 1
- Klypin, A., Kravtsov, A.V., Bullock, J.S., & Primack, J.R. 2001, *ApJ*, 554, 903
- Klypin, A., Zhao, & Somerville, R. 2002, *ApJ*, in press
- Kronawitter, A., Saglia, R.P., Gerhard, O., & Bender, R. 2000, *A&AS*, 144, 53
- Kuntschner, H. 1998, Ph.D. Thesis, 24
- Lauer, T. R. 1985, *ApJS*, 57, 473
- Mahdavi, A. 2001, *ApJ*, 546, 812
- Markevitch, M., Vikhlinin, A., Forman, W.R., & Sarazin, C.L. 1999, *ApJ*, 527, 545
- Miralda-Escudé, J. 1995, *ApJ*, 438, 514
- Miralda-Escudé, J. 2002, *ApJ*, 564, 60
- Moore, B., et al. 1999, *MNRAS*, 310, 1147
- Natarajan, P. & Kneib, J.-P. 1996, *MNRAS*, 283, 1031
- Navarro, J.F., Frenk, C.S., & White, S.D.M. 1997, *ApJ*, 490, 493
- Nusser, A. & Sheth, R.K. 1999, *MNRAS*, 303, 685
- Oke, J.B., et al. 1995, *PASP*, 107, 375
- Peletier, R. F., Davies, R. L., Illingworth, G. D., Davis, L. E., & Cawson, M. 1990, *AJ*, 100, 1091
- Postman, M. & Lauer, T. R. 1995, *ApJ*, 440, 28
- Richstone, D. O. & Tremaine, S. 1984, *ApJ*, 286, 27
- Rines, K., et al. 2000, *AJ*, 120, 2338
- Rix, H., de Zeeuw, P. T., Cretton, N., van der Marel, R. P., & Carollo, C. M. 1997, *ApJ*, 488, 702
- Saglia, R. P., Kronawitter, A., Gerhard, O., & Bender, R. 2000, *AJ*, 119, 153
- Schlegel, D.J., Finkbeiner, D.P., & Davis, M. 1998, *ApJ*, 500, 525
- Schwarzschild, M. 1979, *ApJ*, 232, 236
- Sembach, K.R. & Tonry, J.L. 1996, *AJ*, 112, 797
- Siddiqui, H., Stewart, G.C., & Johnstone, R.M. 1998, *A&A*, 334, 71
- Smith, S. 1935, *ApJ*, 82, 192
- Smith, S. 1936, *ApJ*, 83, 23
- Spiegel, D. N. & Steinhardt, P. J. 2000, *Physical Review Letters*, 84, 3760
- Taylor, J.E., & Navarro, J.F. 2001, *ApJ*, 563, 483
- Tissera, P.B. & Domínguez-Tenreiro, R. 1998, *MNRAS*, 297, 177
- Tonry, J.L. 1983, *ApJ*, 266, 58
- Trager, S.C., Faber, S.M., González, J.J., & Worthey, G. 2000, *AJ*, 120, 165
- Tyson, J.A., Kochanski, G.P., & Dell'Antonion, I.P. 1998, *ApJ*, 498, L107
- van den Bosch, F. C. & Swaters, R. A. 2001, *MNRAS*, 325, 1017
- van der Marel, R.P. & Franx, M. 1993, *ApJ*, 407, 525
- van der Marel, R.P., Magorrian, J., Carlberg, R.G., Yee, H.K.C., & Ellingson, E. 2000, *AJ*, 119, 2038
- Vazdekis, A., Casuso, E., Peletier, R.F., Beckman, J.E. 1996, *ApJS*, 106, 307
- Weinberg, M.D. 2001, *MNRAS*, 328, 321
- Weinberg, M. D. & Katz, N. 2001, *astro-ph/110632*
- Weiner, B. J., Sellwood, J. A., & Williams, T. B. 2001, *ApJ*, 546, 931
- Williams, L.L.R., Navarro, J.F., & Bartelmann, M. 1999, *ApJ*, 527, 535
- Yee, H.K.C., Ellingson, E., & Carlberg, R.G. 1996, *ApJS*, 102, 269
- Yoshida, N., Springel, V., White, S. D. M., & Tormen, G. 2000, *ApJ*, 544, L87
- Zabludoff, A.I., Huchra, J.P., & Geller, M.J. 1990, *ApJS*, 74, 1

TABLE 1
STRUCTURAL PARAMETERS FOR THE STELLAR PROFILE^a

Filter	Correction ^e	$r^{1/4}$ -law ^b		King Model ^c			Power-Law ^d			
		r_e (kpc)	rms (mag)	r_c (kpc)	$r_{1/2}$ (kpc)	Ψ_0/σ^2	rms (mag)	r_c (kpc)	γ	rms (mag)
<i>B</i>	None	61.3	0.073	3.84	102	10.25	0.071	2.35	1.22	0.034
<i>R</i>	None	47.5	0.058	3.58	46.2	9.50	0.069	2.45	1.26	0.048
<i>B</i>	Age	19.7	0.064	2.82	18.2	8.22	0.033	2.94	1.50	0.059
<i>R</i>	Age	19.7	0.052	2.78	18.2	8.23	0.029	2.92	1.49	0.070
<i>B</i>	[Fe/H]	34.2	0.064	3.30	31.6	8.85	0.042	2.66	1.35	0.046
<i>R</i>	[Fe/H]	34.2	0.053	3.28	31.6	8.86	0.051	2.63	1.35	0.055

Note. — ^aTo avoid the effects of the seeing disk, we used an inner fitting radius of $r_{in} = 2''.5$. We also restricted the outer fitting radius to $r_{out} = 75$ kpc because that radius is also the outer radius for the stellar kinematics. ^bThe $r^{1/4}$ -law has been fit so that the resultant half-light (effective) radii can be compared to the half-light radii derived using the other profiles. ^cThe King (1966) profile has two free parameters: r_c , the core radius, and Ψ_0/σ^2 , the truncation energy (see Binney & Tremaine 1987). ^dThe power-law, of the form $\rho \propto [1 + (r/r_c)^2]^{-\gamma}$, has two free parameters as well. Note that because the best-fit power-law profile has $\gamma < 2$, the total mass/luminosity is divergent and there can be no half-light radius. ^eThe color gradient may be interpreted as a spatial variation in the stellar population ages and/or metallicities (see text), and we use this interpretation to explore corrections to the radial variation in (M/L_*) . Even though the color gradient in NGC 6166 is small (see text), the inferred half-mass radii are very sensitive to the correction.

TABLE 2
MAJOR-AXIS KINEMATICS FOR NGC 6166

R (kpc) (1)	ΔR (kpc) (2)	σ (km s^{-1}) (3)	δ_σ (km s^{-1}) (4)	V (km s^{-1}) (5)	δ_V (km s^{-1}) (6)	χ^2 (7)
-17.16	6.29	404.7	47.5	-40.4	34.1	1.36
-12.47	2.61	326.1	59.1	14.0	27.1	1.21
-9.74	2.37	267.1	26.6	-12.3	15.8	1.14
-7.66	1.31	243.6	23.7	-12.7	13.7	1.07
-6.35	0.83	207.1	26.6	-19.8	15.1	1.17
-4.69	2.02	219.9	13.5	-10.1	7.6	1.49
-2.97	0.95	216.7	12.4	-10.9	7.0	1.30
-1.96	0.59	200.3	14.5	0.9	7.5	1.45
-1.25	0.36	215.4	14.4	4.2	7.9	1.27
-0.71	0.24	264.9	14.3	0.7	8.9	1.18
-0.24	0.24	305.7	18.8	-2.6	5.5	1.35
0.24	0.24	289.0	16.9	0.9	6.7	1.27
0.71	0.24	247.2	15.3	-3.9	9.7	1.44
1.25	0.36	209.5	13.1	4.5	8.3	1.39
1.90	0.47	208.2	13.7	-9.2	8.2	1.29
2.73	0.71	217.9	14.2	4.1	7.8	1.18
3.80	0.24	226.4	15.0	-18.7	7.9	1.04
3.86	1.07	216.2	15.4	6.7	8.4	1.20
4.27	0.47	240.8	10.1	-7.1	5.3	1.77
4.93	0.59	220.1	9.3	-2.8	4.6	1.46
5.40	1.54	247.0	16.6	1.5	7.8	1.16
5.58	0.47	197.3	12.0	4.0	5.0	1.34
6.17	0.47	191.6	11.8	17.1	4.8	1.22
7.01	0.95	209.5	11.3	4.0	4.2	1.48
8.01	3.21	233.9	19.6	6.1	7.6	1.12
8.19	1.19	213.0	11.8	-5.6	4.2	1.49
9.44	1.07	221.7	14.8	-10.4	5.5	1.36
10.69	1.19	282.7	15.6	8.1	6.6	1.41
12.05	1.31	262.9	16.1	-27.7	8.0	1.18
13.42	1.42	248.0	16.8	5.3	10.6	1.36
15.67	2.85	275.0	15.3	-4.7	9.4	1.37
18.64	2.85	316.1	17.4	-5.3	11.7	1.25
27.49	2.97	351.1	29.3	38.1	19.5	1.39
30.81	3.44	445.6	60.5	45.0	37.9	1.35
34.91	4.75	490.9	58.6	53.1	29.9	1.72
39.30	4.04	529.1	73.9	114.3	47.3	1.32
57.77	24.34	663.0	121.2	232.6	61.8	2.38

This figure "fig2.png" is available in "png" format from:

<http://arxiv.org/ps/astro-ph/0205316v2>